

<b>REPORT DOCUMENTATION PAGE</b>				<b>Form Approved OMB No. 0704-0188</b>	
<small>Public reporting burden for this collection of information is estimated to average 1 hour per response, including the time for reviewing instructions, searching data sources, gathering and maintaining the data needed, and completing and reviewing the collection of information. Send comments regarding this burden estimate or any other aspect of this collection of information, including suggestions for reducing this burden to Washington Headquarters Service, Directorate for Information Operations and Reports, 1215 Jefferson Davis Highway, Suite 1204, Arlington, VA 22202-4302, and to the Office of Management and Budget, Paperwork Reduction Project (0704-0188) Washington, DC 20503.</small>					
<b>PLEASE DO NOT RETURN YOUR FORM TO THE ABOVE ADDRESS.</b>					
<b>1. REPORT DATE</b> (DD-MM-YYYY) 14-07-2008		<b>2. REPORT TYPE</b> Final		<b>3. DATES COVERED</b> (From - To) 01-04-2004 to 30-05-2008	
<b>4. TITLE AND SUBTITLE</b> Optical Pulse Interactions in Nonlinear Excited State Materials				<b>5a. CONTRACT NUMBER</b>	
				<b>5b. GRANT NUMBER</b> FA9550-04-1-0219	
				<b>5c. PROGRAM ELEMENT NUMBER</b>	
<b>6. AUTHOR(S)</b> Potasek, Mary McLaughlin, David Parilov, Evgueni				<b>5d. PROJECT NUMBER</b>	
				<b>5e. TASK NUMBER</b>	
				<b>5f. WORK UNIT NUMBER</b>	
<b>7. PERFORMING ORGANIZATION NAME(S) AND ADDRESS(ES)</b> Courant Institute of Mathematical Sciences 251 Mercer St. New York University New York, N.Y. 10012				<b>8. PERFORMING ORGANIZATION REPORT NUMBER</b>	
<b>9. SPONSORING/MONITORING AGENCY NAME(S) AND ADDRESS(ES)</b> Dr. Arje Nachman Air Force Office of Scientific Research 875 North Randolph St., Rm 3112 Arlington, VA 22203				<b>10. SPONSOR/MONITOR'S ACRONYM(S)</b> AFOSR/NE	
				<b>11. SPONSORING/MONITORING AGENCY REPORT NUMBER</b>	
<b>12. DISTRIBUTION AVAILABILITY STATEMENT</b> DISTRIBUTION A. Approved for public release; distribution unlimited.					
<b>13. SUPPLEMENTARY NOTES</b>					
<b>14. ABSTRACT</b> We cover five general areas: (1) optical limiting, (2) organic multiphoton absorber (AFX), (3) numerical methods, (4) relationship between the building blocks/decay rate matrix and the coupled propagation/rate equations, and (5) semiconductor quantum dots.					
<b>15. SUBJECT TERMS</b> nonlinear optics, numerical methods, semiconductor quantum dots					
<b>16. SECURITY CLASSIFICATION OF:</b>			<b>17. LIMITATION OF ABSTRACT</b> U	<b>18. NUMBER OF PAGES</b> 64	<b>19a. NAME OF RESPONSIBLE PERSON</b> Dr. M. Potasek
<b>a. REPORT</b> U	<b>b. ABSTRACT</b> U	<b>c. THIS PAGE</b> U			<b>19b. TELEPHONE NUMBER (Include area code)</b> 609-921-1338

## INSTRUCTIONS FOR COMPLETING SF 298

**1. REPORT DATE.** Full publication date, including day, month, if available. Must cite at least the year and be Year 2000 compliant, e.g., 30-06-1998; xx-08-1998; xx-xx-1998.

**2. REPORT TYPE.** State the type of report, such as final, technical, interim, memorandum, master's thesis, progress, quarterly, research, special, group study, etc.

**3. DATES COVERED.** Indicate the time during which the work was performed and the report was written, e.g., Jun 1997 - Jun 1998; 1-10 Jun 1996; May - Nov 1998; Nov 1998.

**4. TITLE.** Enter title and subtitle with volume number and part number, if applicable. On classified documents, enter the title classification in parentheses.

**5a. CONTRACT NUMBER.** Enter all contract numbers as they appear in the report, e.g. F33615-86-C-5169.

**5b. GRANT NUMBER.** Enter all grant numbers as they appear in the report, e.g. 1F665702D1257.

**5c. PROGRAM ELEMENT NUMBER.** Enter all program element numbers as they appear in the report, e.g. AFOSR-82-1234.

**5d. PROJECT NUMBER.** Enter all project numbers as they appear in the report, e.g. 1F665702D1257; ILIR.

**5e. TASK NUMBER.** Enter all task numbers as they appear in the report, e.g. 05; RF0330201; T4112.

**5f. WORK UNIT NUMBER.** Enter all work unit numbers as they appear in the report, e.g. 001; AFAPL30480105.

**6. AUTHOR(S).** Enter name(s) of person(s) responsible for writing the report, performing the research, or credited with the content of the report. The form of entry is the last name, first name, middle initial, and additional qualifiers separated by commas, e.g. Smith, Richard, Jr.

**7. PERFORMING ORGANIZATION NAME(S) AND ADDRESS(ES).** Self-explanatory.

**8. PERFORMING ORGANIZATION REPORT NUMBER.** Enter all unique alphanumeric report numbers assigned by the performing organization, e.g. BRL-1234; AFWL-TR-85-4017-Vol-21-PT-2.

**9. SPONSORING/MONITORS AGENCY NAME(S) AND ADDRESS(ES).** Enter the name and address of the organization(s) financially responsible for and monitoring the work.

**10. SPONSOR/MONITOR'S ACRONYM(S).** Enter, if available, e.g. BRL, ARDEC, NADC.

**11. SPONSOR/MONITOR'S REPORT NUMBER(S).** Enter report number as assigned by the sponsoring/ monitoring agency, if available, e.g. BRL-TR-829; -215.

**12. DISTRIBUTION/AVAILABILITY STATEMENT.** Use agency-mandated availability statements to indicate the public availability or distribution limitations of the report. If additional limitations/restrictions or special markings are indicated, follow agency authorization procedures, e.g. RD/FRD, PROPIN, ITAR, etc. Include copyright information.

**13. SUPPLEMENTARY NOTES.** Enter information not included elsewhere such as: prepared in cooperation with; translation of; report supersedes; old edition number, etc.

**14. ABSTRACT.** A brief (approximately 200 words) factual summary of the most significant information.

**15. SUBJECT TERMS.** Key words or phrases identifying major concepts in the report.

**16. SECURITY CLASSIFICATION.** Enter security classification in accordance with security classification regulations, e.g. U, C, S, etc. If this form contains classified information, stamp classification level on the top and bottom of this page.

**17. LIMITATION OF ABSTRACT.** This block must be completed to assign a distribution limitation to the abstract. Enter UU (Unclassified Unlimited) or SAR (Same as Report). An entry in this block is necessary if the abstract is to be limited.

## Table of Contents

<b><u>Section</u></b>	<b><u>Page</u></b>
<b>List of Figures</b> .....	iv
<b>List of Tables</b> .....	v
<b>1. Executive Summary</b> .....	1
1.1 Introduction.....	1
1.2 List of People involved.....	1
1.3 List of Publications/Reports.....	1
1.4 List of Patents.....	2
<b>2. Introduction to the Project</b> .....	2
2.1 Overview of Optical Limiting .....	2
2.2 Overview of Organic Multiphoton Absorbers (AFX).....	3
2.3 Overview of Numerical Method for the Coupled Propagation/Rate Equations.....	4
2.4 Overview of the Relationship between the Building Blocks and the Coupled Propagation/Rate Equations.....	5
2.5 Overview of Semiconductor Quantum Dots.....	5
<b>3. Results</b> .....	6
3.1 General Numerical Method (Intensity).....	6
3.1.1 Derivation of the theory .....	6
3.1.2 Description of the Generalized Model .....	7
3.1.3 Contributions of Each Electronic Level to the Total Absorption .....	11
3.2 Comparison with Experimental Data (Intensity).....	11
3.2.1 Single photon absorbers .....	12
3.2.2 Two-photon absorbers with excited state absorption .....	16
3.2.3 Three-photon absorbers.....	19
3.3 Femtosecond Duration Pulse Transmission-AF455 (Intensity).....	20
3.3.1 Predictions for AF455 .....	20
3.3.2 Comparison with experiments on AF455.....	22
3.4 General Numerical Method (Electric Field).....	24
3.4.1 Derivation of the theory.....	24
3.4.2 Description of the rate and propagation operators.....	25
3.5 Relationship between the Building Blocks/decay rates and the Coupled Propagation/ Rate Equations.....	26
3.5.1 Energy Level Diagrams and Computational Building Blocks .....	27
3.5.2 Energy Level Diagrams.....	28
3.5.3 Energy Level Criteria.....	29
3.5.4 Absorption/Reverse Absorption Block.....	30
3.5.5 Example of absorption block descriptor.....	31
3.5.6 Stimulated emission.....	31
3.5.7 Absorption blocks and decay rates.....	32
3.5.7.1. Representation of absorption block/decay rate parameters.....	32
3.5.7.2. Examples of inclusion of parameters in matrices and vector.....	33
3.6 Semiconductor Quantum Dots .....	34
3.6.1 Fabrication Techniques .....	34

3.6.1.1 Methods of colloidal synthesis.....	35
3.6.1.2 Core-shell quantum dots.....	35
3.6.1.3 Quantum dot nanostructures.....	35
3.6.1.3.1 Quantum dots on substrates.....	35
3.6.1.3.2 Quantum dots in inorganic matrices.....	35
3.6.1.3.3 Quantum dots in polymers.....	36
3.6.2 Electronic levels of quantum dots.....	36
3.6.3 Generation and recombination of excitons .....	39
3.6.4 Three photoexcitation regions.....	41
3.6.4.1 Case (a) $E \gg E_g$ .....	42
3.6.4.2 Case (b) $E \sim E_g$ .....	43
3.6.4.3 Case (c) $E < E_g$ .....	44
<b>4. Conclusions</b> .....	44
<b>5. References</b> .....	45
<b>Appendix A Description of the Numerical Method</b> .....	49
<b>Appendix B Description of Contribution to Each Energy Level</b> .....	52
<b>Appendix C Numerical Method in terms of Electric Field</b> .....	53

## List of Figures

<b><u>Figure</u></b>	<b><u>Page</u></b>
1. Time scales for various optical limiting effects.....	3
2. Energy-level diagram for AFX chromophores.....	4
3. Basic Blocks. (a) Set of five basics absorption diagrams; (b) reverse absorption diagrams.....	9
4. Energy transmittance as a function of input energy.....	13
5. C <sub>60</sub> nanosecond regime. ....	15
6. AF455 nanosecond regime. ....	17
7. PPAI picosecond regime ....	20
8. Transmission as a function of input energy for AF455 ....	21
9. AF455 femtosecond regime ....	22
10. Experimental energy transmittance of TPA chromophore A455.....	23
11. Extending an existing (5-level) model of AF455 to a new (6-level) model ....	24
12. Energy level diagrams. (a) single electronic level, (b) manifold of states, (c) vibrational and rotational states ....	29
13. Energy level diagram for absorption of $\alpha$ -photons.....	30
14. Green Fluorescent Protein: (a) Jablonski diagram of TPA and ESA. (b) Building Block diagram showing stimulated emission and decay rates ....	31
15. Schematic diagrams of a semiconductor quantum dot (QD): (a) QD alone where each atom is represented by the gold sphere; (b) core/shell structure (QD with organic shell which is represented by the blue lines).....	34
16. Energy level diagrams. (a) bulk semiconductor (b) quantum dot assuming single valence bands.....	36
17. Energy level diagram and transitions for semiconductor quantum dot.....	37
18. Electronic levels for PbSe QDs. (a) Theoretical energy levels as a function of QD size. (b) Theoretical transitions for four QD sizes with experimental transitions shown as dots.....	38
19. Schematic diagram of ground state of a semiconductor quantum dot.....	42
20. Creation of multiple excitons with single high energy photon. The green arrow represents the high energy absorbed photon. (a) Multiple exciton generation (MEG) with phonon decay. The purple curves represent the phonon decays. (b) Carrier multiplication (CM) with Auger recombination. The blue line represents the Coulomb interaction.....	43
21. Creation of a single exciton by an absorbed photon near $E_g$ (a) Lowest energy ( $1S_{3/2}(h)$ to $1S(e)$ ). (b) Higher energy ( $1P_{3/2}(h)$ to $1P(e)$ ).....	43
22. Creation of a single exciton by multiple (2) photons near $E_g$ (a) Lowest energy ( $1S_{3/2}(h)$ to $1S(e)$ ). (b) Higher energy ( $1P_{3/2}(h)$ to $1P(e)$ ).....	44

## List of Tables

<b><u>Table</u></b>	<b><u>Page</u></b>
1. Parameters for multiphoton absorbing materials.....	12
2. Individual contributions to the total absorption of nanosecond pulses to the Electronic states of C <sub>60</sub> .....	15
3. Individual contributions to the total absorption of nanosecond pulses to the electronic states of AF455.....	19
4. Type, description and schematic diagram of various generation and recombination mechanisms of excitons.....	39
5. Properties and mechanisms for three energy regimes in semiconductor quantum dots.....	41

## **1. Executive Summary**

### **1.1 Introduction**

This report describes work performed from 1 April 2004 to 30 May 2008 under AFOSR grant number FA9550-04-1-0219 entitled "Optical Pulse Interactions in Nonlinear Excited State Materials". We cover five general areas: (1) optical limiting, (2) organic multiphoton absorber (AFX), (3) numerical methods, (4) relationship between the building blocks/decay rate matrix and the coupled propagation/rate equations, and (5) semiconductor quantum dots. The introduction to the project and an overview of each area is given in Section 2. Then in Section 3 we present the results for each area. Section 4 contains the conclusion and Section 5 lists the references. There are three detailed appendices of the mathematics at the end.

### **1.2 List of People involved**

M. Potasek, PI

D. McLaughlin, Co-PI

E. Parilov, research associate

Other:

Consultative and advisory functions to other laboratories and agencies

- Consultation and advisory functions to Dr. Chris Brewer, WPAFB/ML, Dr. Ruth Pachter, WPAFB/ML, Dr. Paul Fleitz, WPAFB/ML, Dr. Mark Walker
- Transfer of documentation and results on multiple pulses in femtosecond microlithography, characterization of photosensitive materials for inducing and fabricating novel devices such as photonic crystals, sensors, biosensors, waveguides, MEMS, including numerous conference calls and e-mail communications discussing results with researchers at WPAFB

Transitions

- Transition of new findings and all related materials including related publications to WPAF/ML.

### **1.3 List of Publications/Reports/Presentations**

(a) Referred Publications:

E. Parilov and M. Potasek, "Generalized theoretical treatment and numerical method of time-resolved radially dependent laser pulses interacting with multiphoton absorbers," J. Opt. Soc Amer. B 23, 1894 (2006),

E. Parilov and M. Potasek, "Generalized theoretical treatment and numerical method of time-resolved radially dependent laser pulses interacting with multiphoton absorbers," Virtual Journal of Ultrafast Science, Oct. 2006.

(b) Reports:

M. Potasek and D. McLaughlin, “Optical Pulse Interactions in Nonlinear Excited State Materials”, AFOSR Reports, 2004-2008.

E. Parilov and M. Potasek, “Unifying Approach to Numerical Method for an Electromagnetic Wave Propagating Through a Photoactive Material”, Aug. 2007.

M. Potasek and E. Parilov, “Semiconductor Quantum Dots: Experiments and Theory”, May 30, 2008.

(c) Presentations:

M. Potasek and E. Parilov, “Generalized theoretical treatment and numerical method of time-resolved radially-dependent laser pulses interacting with multi-photon absorbers”, Univ. of Arizona, Oct. 17, 2006.

(d) Participation in Conferences:

- International Symposium on Optical Science and Technology, 49<sup>th</sup> Annual Meeting, 2-6 August 2004, Denver, Colorado
- Conference on Two Photon Absorbers and Nonlinear Optics, Washington, DC, Jan 20, 2004
- Photonics West, San Jose Convention Center, San Jose, CA, Jan. 21-26, 2006
- Photonics West, BIOS, LASE, San Jose Convention Center, San Jose, CA, Jan. 23-25, 2007
- Photonics West, BIOS, OPTO, San Jose Convention Center, San Jose, CA, Jan. 22-26, 2008

## **1.4 List of Patents**

E. Parilov and M. Potasek, “Method, System and Software Arrangement for Determining an Interaction Between an Electromagnetic Radiation and a Material”, US2007/0290147 A1, Dec. 2007.

## **2. Introduction to the Project**

### **2.1 Overview of Optical Limiting**

The general area of nonlinear absorbers/optical limiting has grown substantially over the last two decades. There is increasing interest in various mechanisms of optical limiting. A number of review articles and conference reports demonstrate the vitality of this subject<sup>1-11</sup>. In general, an optical limiter keeps the power, intensity, energy or energy density transmitted by an optical system below a predetermined maximum value that is independent of the size of the input pulse while maintaining a high transmittance at low input power. The many applications of the device include laser power regulation, laser mode-locking, optical pulse shaping, signal level processing, and sensor/detector protection.

Importantly, the device must operate within a fast enough response time to protect a sensor or regulate pulsed laser sources. The transmission must be reduced in a time period shorter than



the pulse width. With laser pulse durations ranging from milliseconds to femtoseconds, electrooptic devices such as electrooptic switches that operate on the nanosecond time scale are often too slow. On the other hand, passive devices use a nonlinear optical medium that has a fast response time and acts as a sensor, processor and modulator<sup>8</sup>. However, typical nonlinear materials are not sufficient optical limiters by themselves. As a result, the passive system places the nonlinear optical components in or near a focal plane. The focal point should be located near the exit plane of the material to utilize the entire path length. The time scale for various optical limiting methods is shown in Fig. 1.

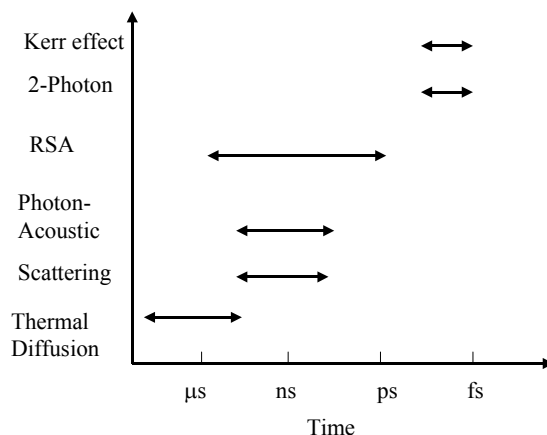


Fig. 1 Time scales for various optical limiting effects.

Optical limiting now requires a sophisticated set of properties including various nonlinear materials, different physical processes, various device designs including a number of lenses and other optical devices, optical pulse shaping, and the characteristics of the laser source including wavelength, pulse duration and pulse repetition rate. This range of materials, processes, and devices involve complex optical propagation requiring a vast diversity of parameters that cannot be fully analyzed without the use of various numerical codes. Along with new materials and device structures, new numerical codes will be key elements in the development of optical limiters. Numerical investigation will be required to make additional advances by examining the various combinations of material, physical, and device parameters that would be too time consuming and/or costly to perform in the laboratory.

Physical mechanisms used in optical limiters include nonlinear refraction, nonlinear scattering, two photon absorption, thermal nonlinearity, and reverse saturable absorption. Materials used in optical limiters include fullerenes, porphyrins, liquid crystals, carbon black and nanostructured materials<sup>1-11</sup>. Various device design and structures also play an important role. Examples of different device design include tandem and graded density structures<sup>7</sup>.

## 2.2 Overview of Organic Multiphoton Absorbers (AFX)

The number of applications for materials exhibiting nonlinear multiphoton behavior has grown significantly in the last two decades. They include safe, high precision diagnostic tools,<sup>12</sup>

effective treatments for various cancer diseases,<sup>13</sup> optical limiters,<sup>14-18</sup> biological detectors,<sup>19</sup> three-dimensional microfabrication,<sup>20-22</sup> fluorescent imaging systems,<sup>23</sup> and optical storage.<sup>24,25</sup>

Because of their importance for a wide range of applications, the design of molecules with large two-photon absorption (TPA) is highly significant.<sup>26</sup> Electron donor-acceptor systems with  $\pi$ -conjugation are often used to enhance the TPA.<sup>26,27</sup> However, it was recognized in the 1970s that the TPA is often followed by excited state absorption (ESA).<sup>28</sup> Furthermore, nonlinear transmission measurements and Z-scan measurements of organic materials show the presence of ESA.<sup>29,30</sup> Recently, a family of D- $\pi$ -A molecules has been introduced for TPA applications, known as the AFX<sup>31</sup>. These chromophores are gathering significant interest for applications in multi-photon processes.

For the AFX group of nonlinear chromophores,<sup>31,32</sup> such simulation is based on the solution of the coupled system of propagation and rate equations with the latter described by a phenomenological five-level absorption model<sup>31</sup> depicted in Fig.2.

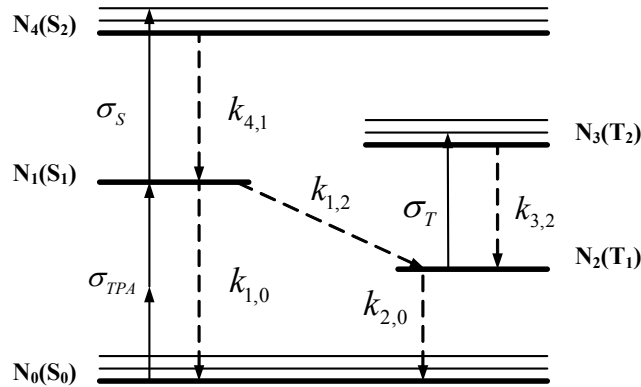


Fig. 2. Energy-level diagram for AFX chromophores. Electronic states are labeled  $N_0 - N_4$ . The upward arrows correspond to photoexcitation transitions and downward arrows correspond to electron decays. The  $\sigma$ 's are absorption cross-sections and the  $k$ 's are the decay rates.

Propagated light may decrease due to TPA, which excites electrons from the ground level  $N_0$  to the singlet excited state  $N_1$ , and/or due to ESA from singlet and/or triplets states  $N_1, N_2$ . Depending on pulse width and intensity of the incident light, the electron population densities change which, in turn, changes the transmittance characteristics of the material.

### 2.3 Overview of Numerical Method

To analyze and predict the experimentally observable behavior of such materials under laser irradiation, one may need to solve a nonlinear system of differential equations. Because not every system may be reduced to a simple form and be solved analytically, it is extremely important to have effective and robust numerical simulation tools. Approximate theories of propagation/transmission through nonlinear materials were designed by researchers in conjunction with their particular experimental data. Many of these approximate theories required numerical solutions; therefore, in order to reduce the computation time several

researchers have used approximate analytic expressions based on some simplifying assumptions. Additionally, because traditional approaches are often used in conjugation with specific laser systems (e.g. specific wavelength and pulse duration) the theoretical/numerical analysis has limited applicability. This aspect often limits the predictive capabilities of the analysis (e.g. a theoretical description for a ns pulsed laser cannot predict the outcome for a ps or fs duration laser system). While traditional approaches have lead to agreement with specific experiments for specific materials, and have yielded significant insight, particularly in absorbers described by single photons processes, we showed that these approaches must be refined and expanded to meet the evolving field of laser transmission through excited state absorbers. In particular, we provided a more general approach for calculating the transmission of laser light through nonlinear absorbers. We use measured parameters - the absorption cross sections and decay rates - in our analysis and do not attempt to derive these parameters either from microscopic quantum mechanical theories or from experimentally measured transmittance data. Rather we establish and derive algorithms for the numerical calculation of macroscopic rate equations including the assumptions and range of applicability of our approach. In order to achieve a more comprehensive numerical method, we introduce the concept of “basic (computational) building block diagrams”.

We described a general numerical method, done in the spirit of the numerical study by Potasek *et al.*,<sup>16</sup> to evaluate the propagation of a short-pulsed laser beam in a multi-level multi-photon absorbing material that includes both multi-photon absorption and one or more single photon excited state absorptions. We outlined a broad spectrum of non-linear materials to which our method can be readily applied, given the photophysical properties of the materials. Our calculations can be performed for pulse widths, which extend from the ns to the fs regime. We validated our technique on a series of nonlinear materials. Because our method is applicable to a wide range of materials and laser systems, it may enable one to use calculations in place of some experiments, which are costly to perform in the laboratory. A new feature of our numerical tool enables us to determine exact contributions of each electronic level to the total absorption, which makes it possible to better explain the roles and relationships between them in complex multi-photon absorbers.

## 2.4 Overview of the Relationship between the Building Blocks/Decay Rate Matrix and the Coupled Propagation/Rate Equations

A more general formulation of the computational “*building blocks*” shown in Fig. 3 can be used to provide information and/or data relating to interactions between electromagnetic waves and “generic” photoactive materials. For example, an “*energy level*” can refer to one or a group of energy states which can contribute to macroscopic physical phenomena such as those described here using mathematical models. Energy levels may apply to atoms, molecules, and/or solids. Such energy levels can include, but are not limited to, electronic, vibrational, rotational, and continuum levels of an atom, molecule, and/or solid, a conduction band, and a valence band of semiconductors and metals. The computational “building blocks” refer to an absorption or inverse absorption (stimulated emission) of an entity including, but not limited to, an electron or an exciton, between different energy levels. The corresponding decay rates appear in the matrix described below.

## 2.5 Overview of Semiconductor Quantum Dot

A quantum dot (QD) is a quasi-zero-dimensional object where the carrier movement is restricted

in three dimensions. The bulk crystalline structure of the semiconductor is maintained in the QD, but they have atomic-like discrete energy states due to 3D confinement. Carrier dynamics in QDs are quite different from bulk materials due to the large energy level spacing and enhanced surface-to-volume ratio.

There are several generation/recombination processes in semiconductors which are described below. A particular process known as the Auger process is non-radiative and is mediated by electron-electron (e-e) Coulomb interactions, which differ amongst atoms, bulk semiconductors and QDs. In atomic systems the e-e coupling is much stronger than the electron-phonon coupling which makes the rates of Auger transitions much greater than the radiative transitions. Thus the decay of multi-electron levels is dominated by Auger processes. However, in bulk semiconductors the efficiency of the Auger process is reduced because the interactions of the electrons are smaller than for QDs. The situation in QDs differs from the bulk in that the quantum confinement enhances the e-e leading to increased Auger rates. Additionally, QDs have a large surface to volume ratio that leads to trap states in the band gap. In many QDs the surface states are passivated by capping the QD with a different semiconductor material or an organic material.

### 3. Results

#### 3.1 General Numerical Method

##### 3.1.1 Derivation of the theory

The wave equation in the presence of the electric polarization vector is given by Maxwell's equation in the scalar form

$$\nabla^2 E(z, r, t) - \frac{1}{c^2} \frac{\partial^2}{\partial t^2} E(z, r, t) = \frac{1}{\epsilon_0 c^2} \frac{\partial^2}{\partial t^2} P(z, r, t). \quad (1)$$

where we assume that  $\nabla \cdot E = 0$ ,  $\epsilon_0$  is the permittivity and  $c$  is the speed of light in vacuum. The optical field  $E$  and the induced nonlinear polarization  $P$  are given by

$$\begin{aligned} E_c(z, r, t) &= \frac{1}{2} \tilde{E}(z, r, t) \exp[-i(\omega_0 t - k_0 z)] + c.c. \\ P_c(z, r, t) &= \tilde{P}(z, r, t) \exp[-i(\omega_0 t - k_0 z)] + c.c. \end{aligned} \quad (2)$$

where  $\omega_0(k_0)$  is the frequency (wave number) of the incident electromagnetic field, and  $\tilde{E}(z, r, t)$  and  $\tilde{P}(z, r, t)$  are the slowly varying envelope of the electromagnetic field and the slowly varying polarization vector, respectively. Then by using the well-know slowly varying envelope approximation (SVEA),<sup>33</sup> i.e. the pulse envelope varies slowly in time compared to an optical period, and the paraxial approximation,<sup>33</sup> i.e. assuming that the envelope is slowly varying along the propagation direction, we can rewrite the scalar wave equation in the form

$$\left( \frac{\partial}{\partial z} + \frac{1}{c} \frac{\partial}{\partial t} - \frac{i}{2k} \nabla_{\perp}^2 \right) \tilde{E}(z, r, t) = \frac{ik}{\epsilon_0} \tilde{P}(z, r, t), \quad (3)$$

where  $\nabla_{\perp}^2$  is the operator for the transverse variables and  $k$  is the frequency dependent wave vector. The intensity of the light is defined by  $\tilde{I}(z, r, t) = cn\epsilon_0 |\tilde{E}(z, r, t)|^2$ , where  $n$  is the linear

index of refraction, and the photon flux at the carrier frequency  $\omega_0$  is defined by  $\tilde{\phi}(z, r, t) = \tilde{I}(z, r, t) / \hbar \omega_0$ . The incident intensity of the laser pulse is given by  $\tilde{I}(z=0, r, t) = \tilde{I}_0 f(r, t)$  where  $f(r, t)$  describes the radial and temporal shape of the incident pulse whose peak value is  $\tilde{I}_0$ .

The polarization vector for the chromophore can be described by the density matrix.<sup>34-37</sup> The Hamiltonian  $\hat{H}$  of the system is described by the unperturbed Hamiltonian  $\hat{H}_0$  and the Hamiltonian  $\hat{H}_{\text{int}}$  (i.e. perturbation term) such that  $\hat{H} = \hat{H}_0 + \hat{H}_{\text{int}}$ .  $\hat{H}_{\text{int}}$  expresses the interaction of light with the molecular system by using the electric-dipole approximation<sup>7</sup>  $\hat{H}_{\text{int}} = -\mathbf{d} \cdot \mathbf{E} \equiv -d E$ , where  $\mathbf{d}$  is the electric-dipole operator, assuming that a laser is linearly polarized, and  $\mathbf{d}$  and  $\mathbf{E}$  both are aligned along x axis. The eigenvalue and eigenenergy for the n-th level is  $|n\rangle$  and  $\varepsilon_n$ , respectively,<sup>38</sup> then the wave function and unperturbed Hamiltonian can be written as  $|\psi\rangle = \sum_n a_n |n\rangle$ ,  $\hat{H}_0 |n\rangle = \varepsilon_n |n\rangle$ . The density matrix operator is defined as  $\hat{g} = |\psi\rangle\langle\psi|$ , and the equation of motion is

$$\frac{\partial \hat{g}}{\partial t} = \frac{-i}{\hbar} [\hat{H}, \hat{g}], \text{ or } \frac{\partial g_{jk}}{\partial t} = \frac{-i}{\hbar} \sum_l (H_{jl} g_{lk} - g_{kl} H_{lj}), \quad (4)$$

where the matrix elements  $g_{jk}$  correspond to a polarization induced by a transition between energy levels  $j$  and  $k$ . Photons from the incident light are absorbed by the molecular system which enables the atoms/molecules to occupy their excited energy states (electron, vibrational, and rotational). Then the polarization for  $n_a$  atoms/molecules per unit volume, where  $R$  describes the distance of the separated charges in the dipole moment approximation, is given by

$$\tilde{P} = n_a \hat{e} \cdot \int \psi \psi^* \vec{R} d\vec{R} = n_a \sum_{jk} g_{jk} d_{kj} = n_a \text{Tr}(dg), \quad (5)$$

where  $\hat{e}$  is the unit electric charge. After excitation to higher energy states, the system relaxes to the ground state through radiative and nonradiative transitions. In the semi-classical case the relaxation terms are added to the equations of motion of the density matrix phenomenologically. In general, the quantum mechanical calculations of the relaxation terms are quite involved.<sup>39-41</sup>

For an understanding of the behavior of an ensemble of radiators (e.g. atoms, molecules, excitons, impurities in a crystal) in a field of resonant or nonresonant electromagnetic waves it is beneficial to characterize the time scales of the various processes. The interaction of the radiators with non-resonant atoms (solvent) can give rise to a dephasing rate,  $\gamma_{jk}$ :

$$\frac{\partial g_{jk}}{\partial t} = -(\gamma_{jk} + i\omega_{jk}) g_{jk} + \frac{-i}{\hbar} \sum_l (H_{jl}^{\text{int}} g_{lk} - g_{kl} H_{lj}^{\text{int}}). \quad (6)$$

### 3.1.2 Description of the Generalized Model

As laser intensities increase many organic molecules exhibit multiphoton absorption involving both singlet and triplet states, which are very challenging for an approach based solely on

quantum calculations. As a result a phenomenological model based on spectroscopic and kinetic data, has lead to a description of nonlinear absorbers involving state diagrams or Jablonski diagrams.<sup>42</sup> This model provides a representation for population dynamics leading to the so-called rate equations. The experimental data used in this approach includes the cross section of absorption and decay rates of the various electronic levels.

Using the analysis described so far allows us to encompass a large group of nonlinear materials which may be characterized by applying one general numerical method. In fact, there are several types of absorption mechanisms within nonlinear materials depending on the number of photons absorbed simultaneously and on which states absorption occurs. Even though our method can be used for N-photon absorbers with both singlet and triplet levels, we limit our examples to at most three photon absorption materials in order to compare our numerical method to experiments. In this way we can distinguish five different types of absorption mechanisms which are depicted on Fig. 3(B<sub>0</sub>)-(B<sub>4</sub>) as transition diagrams. According to the selection rules, single photon absorption may happen along singlet-singlet transitions from ground and/or lowest excited state (Fig. 3(B<sub>0</sub>),(B<sub>1</sub>)), and/or along triplet-triplet transition (Fig. 3(B<sub>2</sub>)) from the lowest triplet excited state which is populated by electrons relaxed along the intersystem crossing link (here we do not take into account ultrafast relaxations happening from the vibronic intermediate states). TPA occurs from the ground state by simultaneous absorbing two photons, and it promotes electrons to the lowest excited singlet state (Fig. 3(B<sub>3</sub>)) with two possible following transitions: singlet-singlet (Fig. 3(B<sub>1</sub>)) or singlet-triplet (Fig. 3(B<sub>2</sub>) from  $N_1$  to  $N_3$ ). Finally, three-photon absorption (3PA) involves promotion of ground state electrons to the lowest excited singlet state by simultaneous absorption of three photons (Fig. 3(B<sub>4</sub>)).

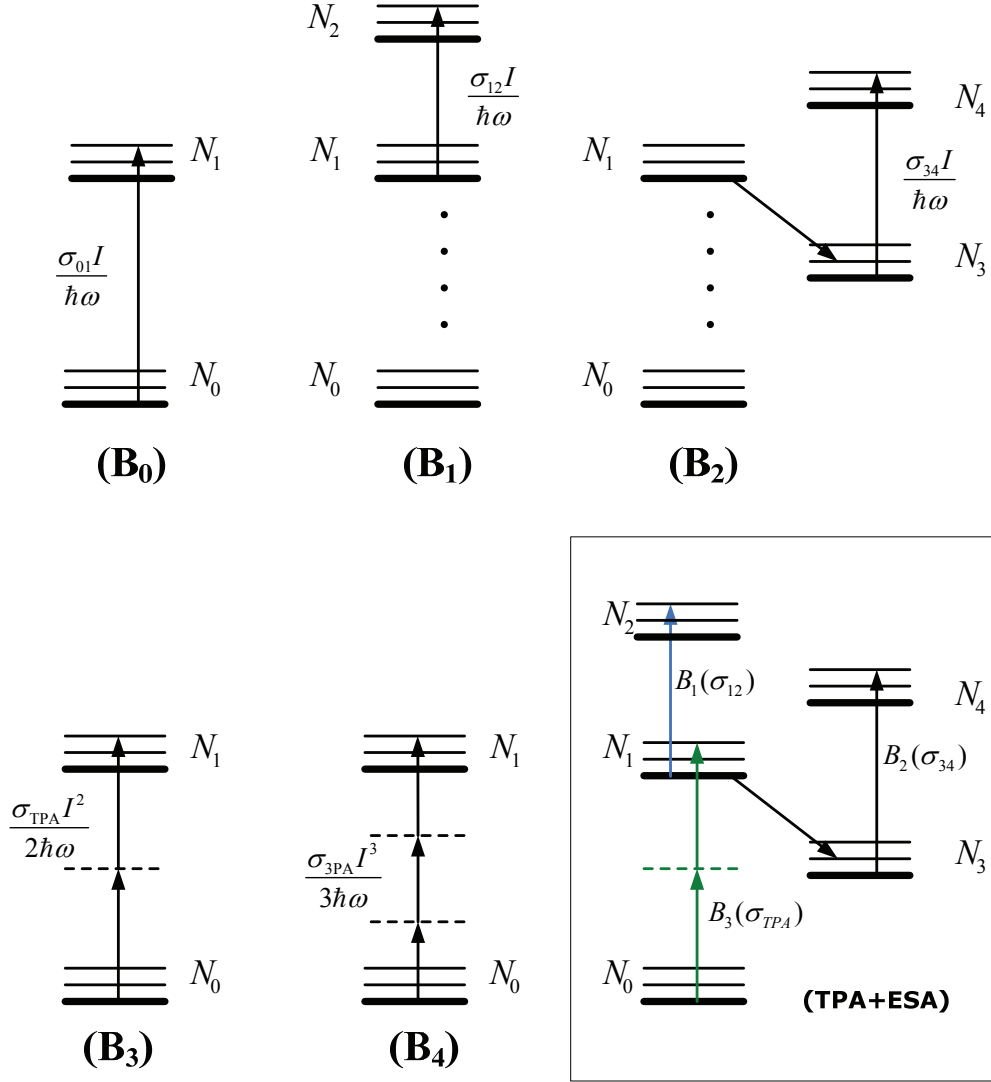


Fig. 3(a). Set of five basics absorption diagrams: **B<sub>0</sub>-B<sub>4</sub>**. Electronic states are labeled  $N_0 - N_4$ , and the  $\sigma$ 's are absorption cross-sections. The upward arrows correspond to photo-excitation transitions and downward arrow correspond to intersystem electron decay (for simplicity, we omit all other possible singlet-singlet and triplet-triplet states electron decays). Inset in the bottom right corner depicts representation of a TPA-ESA material within our framework of building basic blocks **B<sub>0</sub>-B<sub>4</sub>**.

Fig. 3 (b). Set of three basic stimulation emission diagrams **B<sub>5</sub>**, **B<sub>6</sub>**, and **B<sub>7</sub>**. Similar to Fig. 3 (a) except that the downward arrow corresponds to reverse absorption in which one (or,  $\alpha > 1$ ) photon(s) is (are) emitted from  $N_1$  to  $N_0$ : number of photons reversely absorbed is specified as a superscript of the absorption cross-section with negative value  $-\alpha$  (this distinction is made due to the fact that in many cases cross-sections of absorption and stimulation emission are not the same,  $\sigma_{TPA} \neq \sigma_{TPA}^{(-2)}$ ).

Diagrams B<sub>0</sub>-B<sub>7</sub> in Fig. 3 may be considered as basic (computational) building blocks for describing such materials. By combining “related” diagrams one can get description of many existing nonlinear materials. For example, one can describe the five-level model of C<sub>60</sub>-toluene solution<sup>43</sup> - nonlinear RSA material - by merging diagrams  $B_0 \cup B_1 \cup B_2$ ; or describe the five-level model of a chromophore from AFX group<sup>32</sup> exhibiting TPA assisted excited state absorption by combining diagrams  $B_1 \cup B_2 \cup B_3$  which is depicted on Fig. 3(TPA+ESA). We will call nonlinear material *generic* if its energy diagram may be composed from our set of basic diagrams B<sub>0</sub>-B<sub>7</sub>.

A valid diagram composed from the introduced set of transition diagrams uniquely defines the rate and propagation equations. According to the derivation described in the beginning of this section and in Appendix A the rate equation in the moving time frame ( $z, t = t' - k_1 z$ ) for a material which falls in our generic category can be expressed in the matrix form written as

$$\frac{d\tilde{\mathbf{N}}(z, r, t)}{dt} = \left[ \hat{D}_0 + \sum_{\alpha=1}^{N_A} \frac{\hat{D}_\alpha}{\alpha \hbar \omega_0} \tilde{I}^\alpha(z, r, t) \right] \tilde{\mathbf{N}}(z, r, t), \quad (7)$$

where  $\tilde{\mathbf{N}} = [\tilde{N}_0, \tilde{N}_1, \dots, \tilde{N}_s]^T$  is a population density vector function  $\tilde{\mathbf{N}}(z, r, t)$  for a system with  $s$  electronic levels,  $\hat{D}_0 \equiv \hat{D}_0(\{k_{ij}, 0\})$ ,  $\hat{D}_1 \equiv \hat{D}_1(\{\sigma_{ij}, \sigma_{i'j'}^{(-1)}\})$ ,  $\hat{D}_2 \equiv \hat{D}_2(\{\sigma_{TPA}, \sigma_{TPA}^{(-2)}\})$ ,  $\hat{D}_3 \equiv \hat{D}_3(\{\sigma_{3PA}, \sigma_{3PA}^{(-3)}\})$ , ...,  $\hat{D}_{N_A} \equiv \hat{D}_{N_A}(\{\sigma_{[N_A]PA}, \sigma_{[N_A]PA}^{(-N_A)}\})$  are  $N_A + 1$  constant  $s \times s$  sparse matrices of decay rates  $k_{ij}$ , single photon  $\sigma_{ij}$ , two-photon  $\sigma_{TPA}$ , three-photon  $\sigma_{3PA}$ , and, possibly,  $N_A$ -photon  $\sigma_{[N_A]PA}$  molar absorption cross-sections correspondingly, and  $\tilde{I}(z, r, t)$  is a function of photon flux density. The propagation equation for such material is given in the vector form by



$$\frac{d\tilde{I}(z, r, t)}{dz} = -\sum_{\beta=1}^{N_B} (\boldsymbol{\sigma}_\beta \cdot \tilde{\mathbf{N}}(z, r, t)) \tilde{I}^\beta(z, r, t), \quad (8)$$

with  $\boldsymbol{\sigma}_1 \equiv \boldsymbol{\sigma}_1(\{\sigma_{ij}, \sigma_{i'j'}^{(-1)}\})$ ,  $\boldsymbol{\sigma}_2 \equiv \boldsymbol{\sigma}_2(\{\sigma_{TPA}, \sigma_{TPA}^{(-2)}\})$ ,  $\boldsymbol{\sigma}_3 \equiv \boldsymbol{\sigma}_3(\{\sigma_{3PA}, \sigma_{3PA}^{(-3)}\})$ , ...,  $\boldsymbol{\sigma}_{N_B} \equiv \boldsymbol{\sigma}_{N_B}(\{\sigma_{[N_A]PA}, \sigma_{[N_A]PA}^{(-N_A)}\})$  are  $N_B$  constant (mostly sparse)  $s$  dimensional vectors composed of certain elements of corresponding  $\hat{D}_\beta$  matrices.

A better understanding of the characteristics of the numerical scheme for Eqs.(7) and (8) can be obtained by first making it dimensionless using the following transformations  $\eta = z/L_{df}$ ,  $\rho = r/R_0$ ,  $\tau = t/T_0$ ,  $I(\eta, \rho, \tau) = \tilde{I}(\eta, \rho, \tau)/I_0$ ,  $N_\beta(\eta, \rho, \tau) = \tilde{N}_\beta(\eta, \rho, \tau)/N$ ,  $L_{df} = \pi R_0^2 n_1/\lambda$ ,  $I_0$  is the peak intensity. Here  $T_0$ ,  $R_0$  are pulse width and beam radius described by the incident pulse shape, and  $N$  is the total population electron density of the material, which is constant for all times,  $N = \sum_\beta \tilde{N}_\beta(\eta, \rho, \tau)$ . The incident pulse can be described by the general formula given by  $I(\eta = 0, \rho, \tau) = I_0 f(\rho, \tau)$ , e.g.,  $f(\rho, \tau) = \exp(-\tau^2) \exp(-\rho^2)$  for the standard Gaussian shape.

Using the transformations described above, Eqs. (7) and (8) are given by

$$\frac{d\mathbf{N}(\eta, \rho, \tau)}{d\tau} = T_0 \left[ \hat{D}_0 + \sum_{\alpha=1}^{N_A} \frac{\hat{D}_\alpha I_0^\alpha}{\alpha \hbar \omega_0} I^\alpha(\eta, \rho, \tau) \right] \mathbf{N}(\eta, \rho, \tau), \quad (9)$$

$$\frac{dI(\eta, \rho, \tau)}{d\eta} = -L_{df} N \sum_{\beta=1}^{N_B} (\boldsymbol{\sigma}_\beta \cdot \mathbf{N}(\eta, \rho, \tau)) I_0^{(\beta-1)} I^\beta(\eta, \rho, \tau), \quad (10)$$

respectively. The analysis involves the solution of Eqs. (9) and (10). A description of the numerical method is given in Appendix A. Within the framework of basic blocks B<sub>0</sub>-B<sub>7</sub> the constants  $N_A$  and  $N_B$  are restricted to be  $N_A \leq 3$  and  $N_B \leq 3$ .

### 3.1.3 Contributions of Each Electronic Level to the Total Absorption

We introduce a new feature into our numerical scheme that characterizes the materials from our generic category, enabling an investigator to obtain a more systematic analysis of the material's nonlinear properties. This feature is the exact contributions from each electronic level to the total absorption. Usually such contributions are roughly deduced from the dynamics of the population densities of electronic levels. However, relative contributions do not always match the corresponding relative population densities, so that the approximations of such contributions solely based on the population densities may be too far from the actual values. Our numerical solution allows us for any propagation distance, radius, and time step to obtain both the population density values and intensity absorption due to each electronic level, so that we calculate precisely the relative contributions to the total absorption. Appendix B gives the detailed mathematical analysis of the contribution of each electronic level to the total absorption.

## 3.2. Comparison with Experimental Data

We selected a group of nonlinear materials, and validated our numerical scheme against their transmittance data measured in different lasing conditions. Our choice of materials was mainly

motivated by a desire to choose key representatives from the possible generic materials described here. Among the single photon absorbers, we picked  $C_{60}$ -toluene solution,<sup>43</sup> which exhibits reverse saturable absorption; for the two-photon absorbers, we chose AFX chromophore AF455;<sup>14,31</sup> and we selected PPAI dye<sup>44</sup> for the 3PA materials. These materials attracted a lot of attention in recent years because of their promising nonlinear optical properties.

Comparison of theory with experiments requires a definition of  $f(\rho, \tau)$ . The analytical and numerical techniques explained above assumed a Gaussian function for  $f(\rho, \tau)$ , which well describes the pulse shapes from the lasers used in the experiments. Therefore the incident laser intensity is given by

$$I(\eta = 0, \rho, \tau) = I_0 \exp(-\tau^2) \exp(-\rho^2). \quad (11)$$

### 3.2.1. Single photon absorbers

The first chosen nonlinear material,  $C_{60}$ , belongs to the group of reverse saturable absorbers – the materials with ESA cross sections being much higher than that of the ground state – with the energy diagram  $B_0 \cup B_2 \cup B_3$ , which uniquely defines the vectors and matrices of the coefficients for the rate/propagation Eqs. (7) and (8) given by:

$$\begin{aligned} \boldsymbol{\sigma}_1 &= [\sigma_{01}, \sigma_{12}, 0, \sigma_{34}, 0], \quad \boldsymbol{\sigma}_2 = \boldsymbol{\sigma}_3 = \mathbf{0} \\ \hat{D}_0 &= \begin{pmatrix} 0 & k_{10} & 0 & k_{30} & 0 \\ 0 & -(k_{13} + k_{10}) & k_{21} & 0 & 0 \\ 0 & 0 & -k_{21} & 0 & 0 \\ 0 & k_{13} & 0 & -k_{30} & k_{43} \\ 0 & 0 & 0 & 0 & -k_{43} \end{pmatrix}, \quad \hat{D}_1 = \begin{pmatrix} -\sigma_{01} & 0 & 0 & 0 & 0 \\ \sigma_{01} & -\sigma_{12} & 0 & 0 & 0 \\ 0 & \sigma_{12} & 0 & 0 & 0 \\ 0 & 0 & 0 & -\sigma_{34} & 0 \\ 0 & 0 & 0 & \sigma_{34} & 0 \end{pmatrix}, \\ \hat{D}_2 &= \hat{D}_3 = (0)_{5 \times 5}, \end{aligned} \quad (12)$$

where all the coefficients as well as experimental parameters, due McLean *et al.*<sup>43</sup>, are collected in Table 1.

Table 1. Parameters for multiphoton absorbing materials.

	$C_{60}$ -toluene solution <sup>a</sup>	AF455 chromophore <sup>b</sup>	PPAI dye <sup>c</sup>
$\sigma_{3PA} \text{ (cm}^3 / \text{W}^2 \text{)}$			$3.2 \times 10^{-21}$
$\sigma_{TPA} \text{ (cm}^4 / \text{GW} \text{)}$		$0.5 \times 10^{-20} \text{ d}$	
$\sigma_{01} \text{ (cm}^2 \text{)}$	$3.1 \times 10^{-18} \text{ e}$		
$\sigma_{12} \text{ (cm}^2 \text{)}$	$1.6 \times 10^{-17}$	$1.68 \times 10^{-17}$	
$\sigma_{34} \text{ (cm}^2 \text{)}$	$1.4 \times 10^{-17}$	$17.1 \times 10^{-17}$	
$k_{10}^{-1} \text{ (ns)}$	32.5	2.72	
$k_{21}^{-1} \text{ (ps)}$	1.0	$1.66 \text{ f}$	
$k_{13}^{-1} \text{ (ns)}$	1.35	45.3	

$k_{30}^{-1}$ ( $\mu\text{s}$ )	40.0 <sup>g</sup>	0.368	
$k_{43}^{-1}$ (ps)	1.0 <sup>f</sup>	10.0 <sup>g</sup>	
$z_{\text{max}}$ (mm)	1.0	1.0	10.0
$L_{df}$	0.37306	2.24	0.8059
$N_T$ ( $\text{nm}^{-3}$ )	$1.559 \times 10^{-3}$ <sub>h</sub>	0.012 <sup>i</sup>	$0.596 \times 10^{-3}$ <sup>k</sup>
Energy levels diagram	$B_0 \cup B_1 \cup B_2$	$B_1 \cup B_2 \cup B_3$	$B_4$
$R_0$ ( $\mu\text{m}$ )	16.687 <sup>m</sup>	9.25	53.315
$T_0$ (ns)	9.608	2.71	$2.474 \times 10^{-2}$
$\lambda_0$ (nm)	532	800	1064

<sup>a</sup> Most of the parameters were taken from Ref. 45, experimental parameters are described in Ref. 43

<sup>b</sup> Material and measurement parameters are described in the experimental section of Ref. 31

<sup>c</sup> Ref. 44

<sup>d</sup> Refs. 32,45

<sup>e</sup> Ref. 43

<sup>f</sup> Ref. 14

<sup>g</sup> Ref. 28

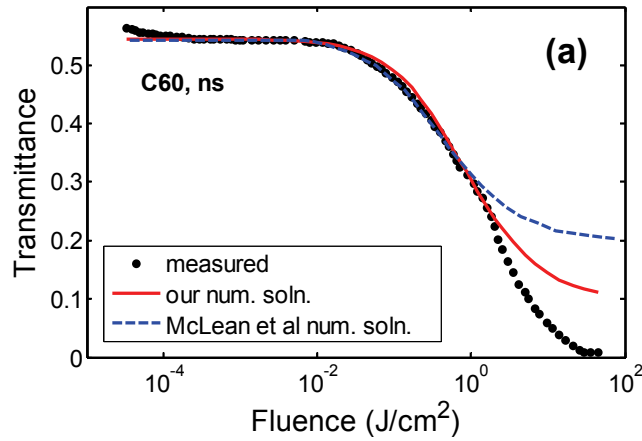
<sup>h</sup> Corresponds to 2.59mM solution of C<sub>60</sub> in toluene

<sup>i</sup> Corresponds to 0.02M

<sup>k</sup> Corresponds to 0.99mM of the dye in DMSO

<sup>m</sup> All laser parameters are deduced from the corresponding original parameters by using Eq. (11)

We used the iterating scheme given by Eqs. (A5) and (A6) (See Appendix A.) with  $K = 2$ , and achieved an excellent match with the measured transmittance data<sup>42</sup> within the input fluence range  $[3.6 \times 10^{-5}, 5.0]$  J/cm<sup>2</sup> ( Fig. 4(a)).



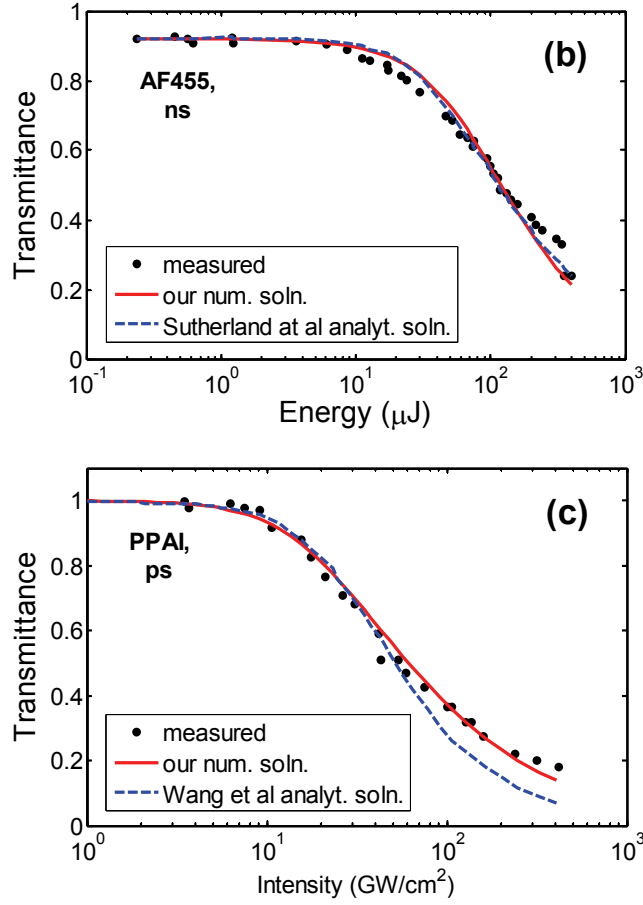


Fig. 4. Energy transmittance  $T_E$  as a function of input energy. The measured data is shown by the • (dot) symbol, the solid line is our numerical calculation; the dashed line is the original solution. (a) Comparing with the numerical solution of McLean *et al.*<sup>43</sup> for  $\text{C}_{60}$ , ns; (b) comparing with the analytical calculation of Sutherland *et al.*<sup>31</sup> AF455, ns; (c) comparing with the analytical calculation of Wang *et al.*<sup>44</sup> PPAI, ps. All the parameters are given in the Table 1.

Because the analytical solution of Eqs. (7) and (8) in Ref. 42 is less accurate in describing the evolution of the population densities at high fluence inputs than our complete numerical integration, our solution is noticeably better for fluence values above  $1.4 \text{ J}/\text{cm}^2$ . Neither solution, however, matches the measured data above  $5.0 \text{ J}/\text{cm}^2$  (McLean *et al.*<sup>42</sup> noticed experimentally damage at high input energy). According to the values of the individual contributions collected in Table 2 (see definitions in Appendix B), the nonlinear transmittance of  $\text{C}_{60}$  in the ns regime is mostly attributed to the lowest triplet-triplet state absorption varying from 71% to 99.8% depending on the input energy value.

Table 2. Individual contributions to the total absorption of nanosecond pulses to the electronic states of  $C_{60}$ .

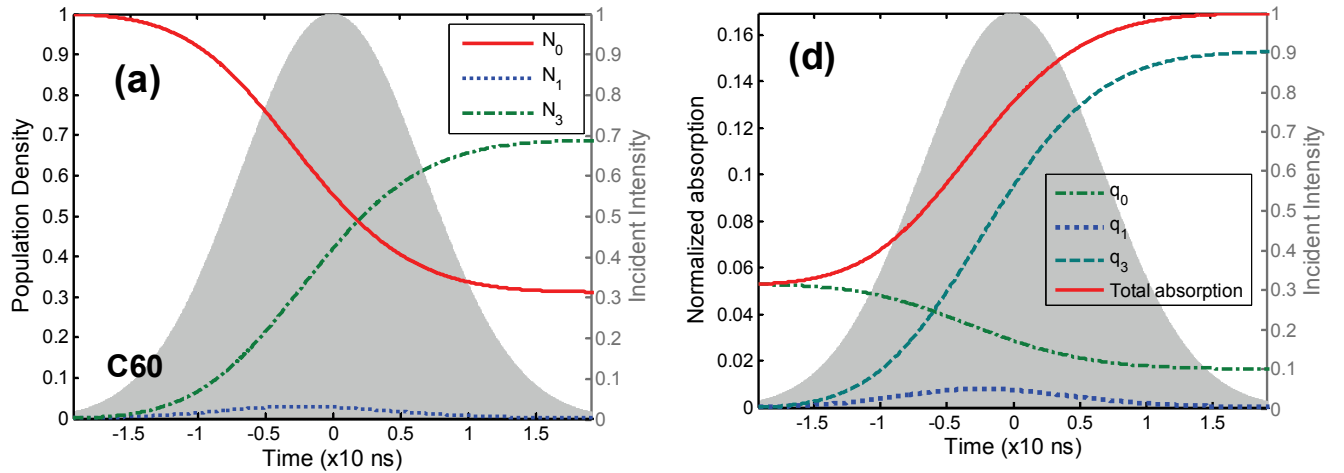
Levels\ $\Phi_{in} (J/cm^2)$	0.51 <sup>a</sup> ( $\approx 4.5 \mu J$ )			2.05 ( $\approx 17.9 \mu J$ )			14.1 ( $\approx 123.0 \mu J$ )		
$\langle \hat{p}_0 \rangle^b$	79.2	23.1	10.4	50.3	4.0	0.3	15.9	0.0	0.0
$\langle \hat{p}_1 \rangle$	3.8	5.1	0.7	8.5	3.6	0.1	9.8	0.1	0.0
$\langle \hat{p}_3 \rangle$	16.9	71.7	88.8	41.0	92.3	99.5	74.2	99.8	99.9
$\langle q \rangle^c$	0.06	0.13	0.17	0.08	0.19	0.21	0.14	0.21	0.21

<sup>a</sup> For a given input fluence value, we calculated three values (left, middle, and right columns) corresponding to the relative contributions to the absorption averaged within every element of the  $\tau$ -range partition:  $[-1, -1/3]$ ,  $[-1/3, 1/3]$ , and  $[1/3, 1]$ .

<sup>b</sup> Relative contribution to the absorption for level 0

<sup>c</sup> Averaged intensity decay values.

But in addition to  $N_3$ , the ground level contributes  $\sim 23\%$  to the total absorption at low input intensities, and this contribution is lost at higher intensities because of the fast bleaching of the ground level (see dynamics of the population densities and individual contributions in Fig. 5). This explains the excellent match between calculations and experiments below  $1.4 J/cm^2$ , acceptable match below  $5.0 J/cm^2$ , but poor match of both methods above  $5.0 J/cm^2$ . Material degradation at high input intensities is another possible reason for the divergence of numerical solutions, based on integration of the rate-propagation equations, from the measured data.



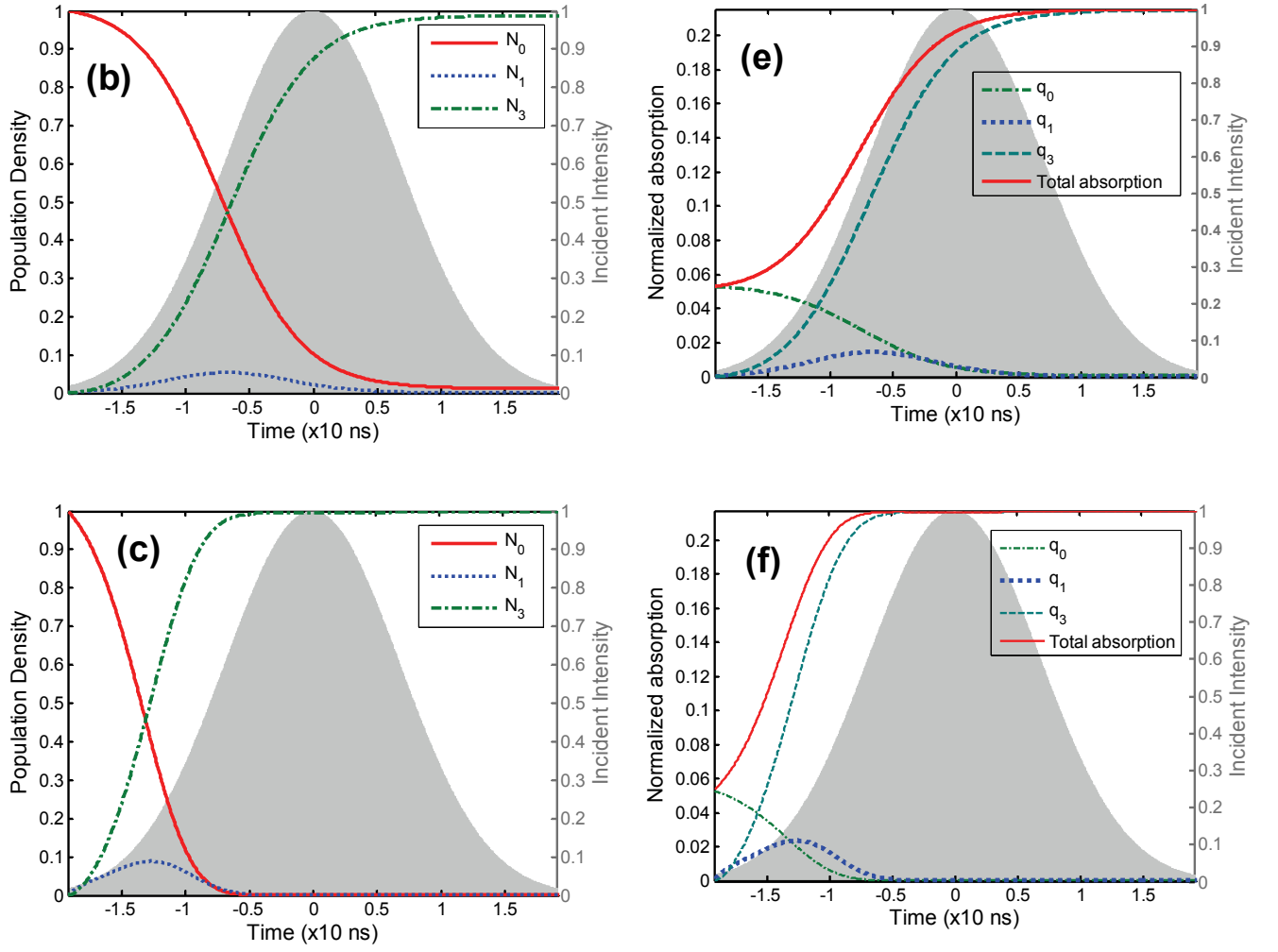


Fig 5.  $C_{60}$  nanosecond regime. Evolution of population densities (left column) and absolute contributions (right column) due different active electronic levels superimposed with the total absorption at the entrance of the slab,  $\eta = 0$ , and at  $\rho = 0$  for different incident fluence values:  $\Phi_{in} = \{0.51, 2.05, 14.1\}$  given in  $[J/cm^2]$  (from top to bottom, correspondingly).

### 3.2.2. Two-photon absorbers with excited state absorption

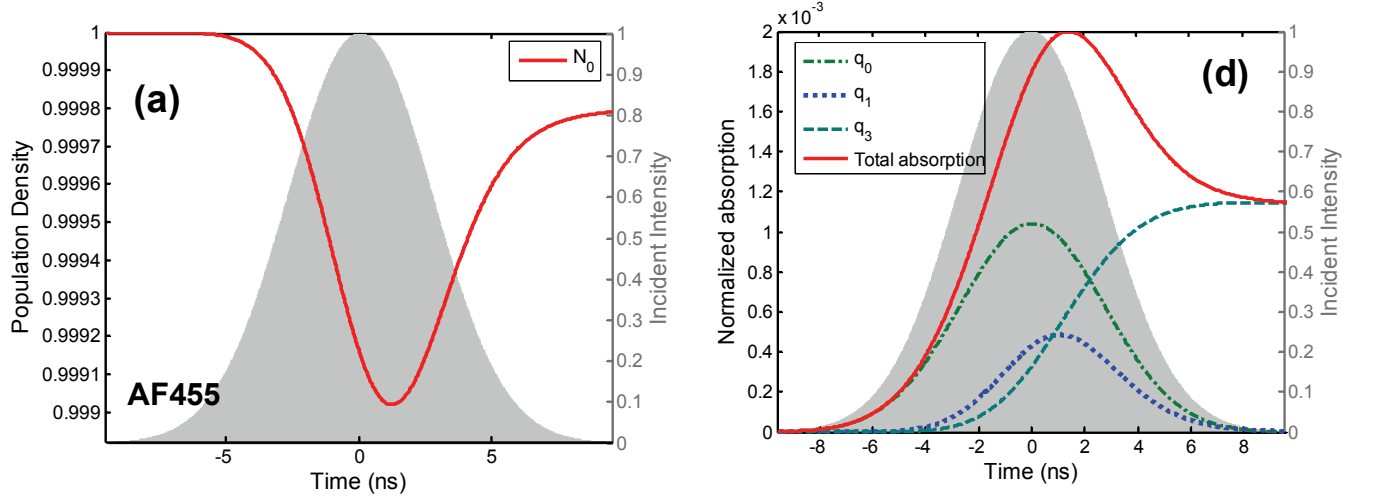
A theoretical basis for and experimental results on nonlinear transmittance in the ns regime of D- $\pi$ -A chromophore AF455 – a material which exhibits two-photon assisted ESA – was presented by Sutherland *et al.*<sup>31</sup> Within our classification, its energy levels diagram is composed of TPA and single photon absorption basic blocks:  $B_1 \cup B_2 \cup B_3$ , and parameters given by:

$$\sigma_1 = [0, \sigma_S, \sigma_T, 0, 0], \sigma_2 = [\sigma_{TPA}, 0, 0, 0, 0], \sigma_3 = \mathbf{0}$$

$$\hat{D}_1 = \begin{pmatrix} 0 & 0 & 0 & 0 & 0 \\ 0 & -\sigma_S & 0 & 0 & 0 \\ 0 & 0 & -\sigma_T & 0 & 0 \\ 0 & 0 & \sigma_T & 0 & 0 \\ 0 & \sigma_S & 0 & 0 & 0 \end{pmatrix}, \hat{D}_2 = \begin{pmatrix} -\sigma_{TPA} & 0 & 0 & 0 & 0 \\ \sigma_{TPA} & 0 & 0 & 0 & 0 \\ 0 & 0 & 0 & 0 & 0 \\ 0 & 0 & 0 & 0 & 0 \\ 0 & 0 & 0 & 0 & 0 \end{pmatrix}, \hat{D}_3 = (0)_{5 \times 5}, \quad (13)$$

where the same matrix  $\hat{D}_0$  as for  $C_{60}$  is used. We ran our technique against the experimental parameters of Sutherland *et al.*<sup>31</sup> (summarized in Table 1), found excellent agreement with the measured data, and observed nearly total coincidence with the previous analytical solution<sup>21</sup> as shown in Fig. 4(b).

According to the plots of the population densities shown in Figs. 6(a), (b) for two chosen input energy values, the depletion of the ground level is almost negligible. It confirms the validity of their steady-state approximation<sup>31</sup> for the population densities in ns regime that explains the excellent match of our numerical solution with their analytical solution. However, for higher input energies this assumption fails, because there is a considerable increase of the population densities  $N_1$  and  $N_3$  as shown in Fig. 6(c) for the ns regime, whereas in fs regime the ground state is depleted rapidly, as shown in Fig. 9(a). Therefore, our numerical solution is more accurate for higher input intensities as it encompasses the dynamics of population densities.



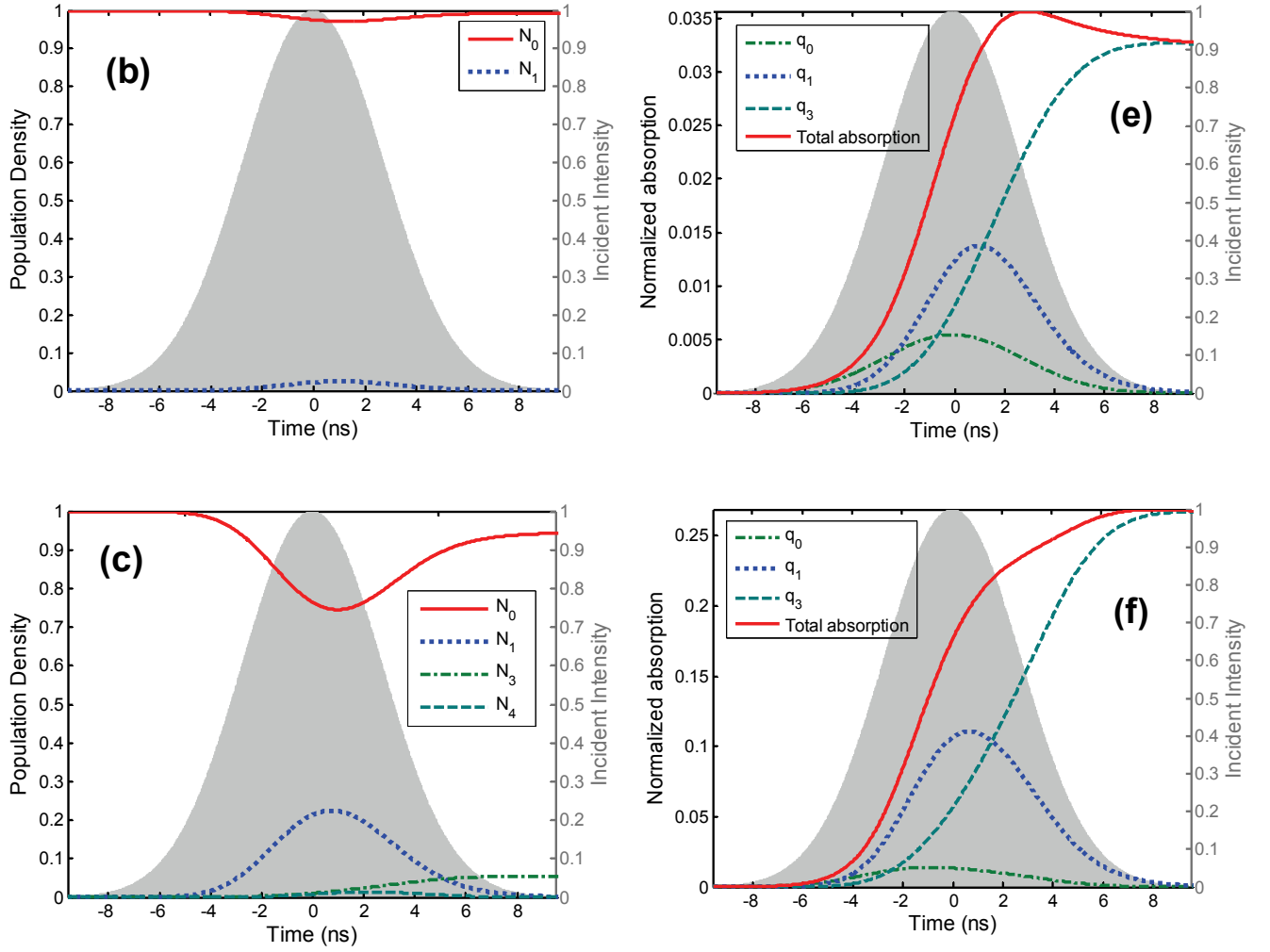


Fig. 6. AF455 nanosecond regime. Evolution of population densities (left column) and absolute contributions (right column) due different active electronic levels superimposed with the total absorption at the entrance of the slab,  $\eta = 0$ , and at  $\rho = 0$  for different incident energy values:  $E_{in} = \{17\mu\text{J}, 93\mu\text{J}, 0.33\text{mJ}\}$  (from top to bottom, correspondingly).

An analysis of the absolute contributions from different electronic levels, whose plots are depicted in Figs. 6(d)-(f), helps one to better understand the absorption within the AF455 sample for ns pulses. The major absorption occurs in the central-to-right part of the propagating pulse, and results in advancing the leading edge of the pulse as it propagations through the sample. For relatively small input energies, the ground level is the main contributor to the total absorption with  $\sim 54\%$  of average contribution inside the central part of the pulse (for details see Table 2 which presents the individual contributions averaged over the leading, central, and trailing parts of the propagating pulse at  $\eta = 0$  for three input energy values). However, the contribution of the ground state TPA for higher energies (Table 3, columns 2 and 3) falls abruptly, and the main



contributors are ESA of the lowest singlet-singlet and the lowest triplet-triplet states with corresponding individual contributions of  $\sim 40\%$  and  $\sim 40.9\%$  for the central part of the pulse, respectively.

Table 3. Individual contributions to the total absorption of nanosecond pulses to the electronic states of AF455.

Levels\ $E_{in}(\mu J)$	17.0			93.0			330.0		
$\langle \hat{p}_0 \rangle$	92.8	54.1	10.2	70.5	18.8	2.1	40.9	7.3	0.7
$\langle \hat{p}_1 \rangle$	5.4	21.2	6.3	22.7	40.2	7.0	47.0	51.3	7.5
$\langle \hat{p}_3 \rangle$	1.7	24.5	83.4	6.7	40.9	90.8	11.9	41.3	91.7
$\langle q \rangle$	1.4e- 4	1.5e- 3	1.3e- 3	1.0e- 3	0.02	0.03	6.0e- 3	0.16	0.26

### 3.2.3. Three-photon absorbers

With the advent of shorter pulsed and higher intensity lasers, three or more photon processes can now be measured.<sup>44</sup> These materials may be of interest in areas such as laser micro-or nano-machining because of their ability to reduce the feature size of structures in substrate materials. In contrast to the previous nonlinear materials, there is little investigation of these materials such as the recently discovered 3PA dye, abbreviated as PPAI.<sup>44</sup> The initial experimental investigation of this material shows a high three-photon absorption cross-section in the near infrared region, so that all the parametric vectors and matrices will be zero, excluding the following two:

$$\sigma_3 = [\sigma_{3PA}, 0], \quad \hat{D}_3 = \begin{pmatrix} -\sigma_{3PA} & 0 \\ \sigma_{3PA} & 0 \end{pmatrix}, \quad (14)$$

and the energy level diagram consists of only one building block B<sub>4</sub> (the setup parameters are in Table 1). Our numerical solution matches extremely well with the transmittance measurements published in Ref. 44 (see transmittance curve in Fig. 4(c)). Moreover, it is even closer to the measurements than the previously published analytic solution of Wang et. al.<sup>44</sup> in the high input intensity region. One obvious reason is that their analytical model assumes constant population density of the ground level. This assumption is reasonable in the low intensity region, which is demonstrated by Fig.7(a). But, in the high intensity region, according to our time-resolved population density solution depicted on Fig. 7(b), this assumption breaks down ( $N_0$  drops more than a half in the second part of the pulse), so that our solution is more complete and reliable. Dynamics of the population density  $N_1$  in Fig. 7(b) also confirms their supposition that excited state absorption may significantly affect the transmittance at high input intensities.

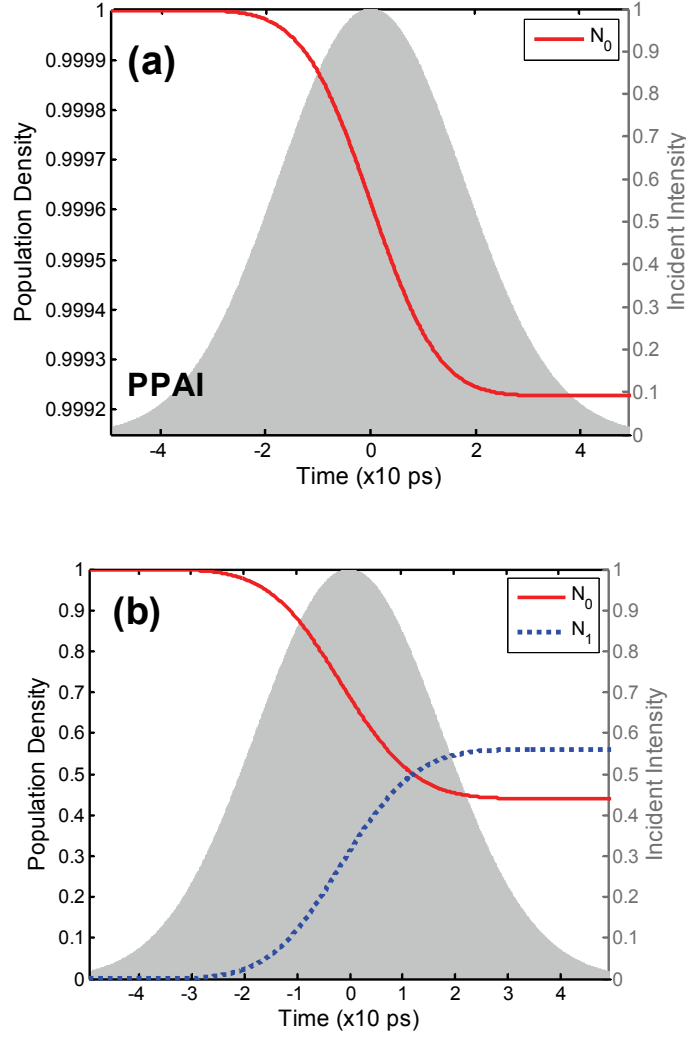


Fig. 7. PPAI picosecond regime. Evolution of the population densities at the entrance of the slab,  $\eta = 0$ , and at  $\rho = 0$  for two incident intensity values:  $I_{\text{in}} = \{16.9, 204.5\}$  given in  $[\text{GW}/\text{cm}^2]$ , which correspond to  $E_{\text{in}} = \{66.4 \mu\text{J}, 0.8 \text{ mJ}\}$ .

### 3.3. Femtosecond Duration Pulse Transmission-AF455

#### 3.3.1. Predictions for AF455

Unlike many previous numerical or analytical techniques, our detailed analysis enables us to investigate many cases of nonlinear absorption including situations that have not been measured, particularly for short-pulsed lasers. The excellent agreement of our calculations with experimental results gives us confidence to use it as a predictive tool for experiments which have not yet been performed. Since the investigation of ultrashort pulses with nonlinear materials is of increasing importance and the short pulse behavior of AF455 has not been quantified yet, we applied our method using a fs laser pulse to predict its effects on the nonlinear transmission of AF455. We assumed a Gaussian pulse with  $R_0 = 5.0 \mu\text{m}$ ,  $T_0 = 144.0 \text{ fs}$ , and  $\lambda_0 = 800 \text{ nm}$  and

obtained  $\sim 0.002$  transmittance at the exit of the AF455 slab ( $z_{\max} = 3.0L_{df} \approx 0.412$  mm) for input energies  $\sim 10.0 \mu\text{J}$  (See transmittance plot for different input energy values in Fig. 8.). This transmittance value is almost two orders of magnitude smaller than that obtained by using ns pulses. By increasing the slab thickness, one can hypothetically achieve even less transmittance, which makes AF455 an ideal candidate for high intensity nonlinear absorbers. With further validation, our numerical method may enable one to substitute calculations for many laboratory experiments, which are both costly and time-consuming.

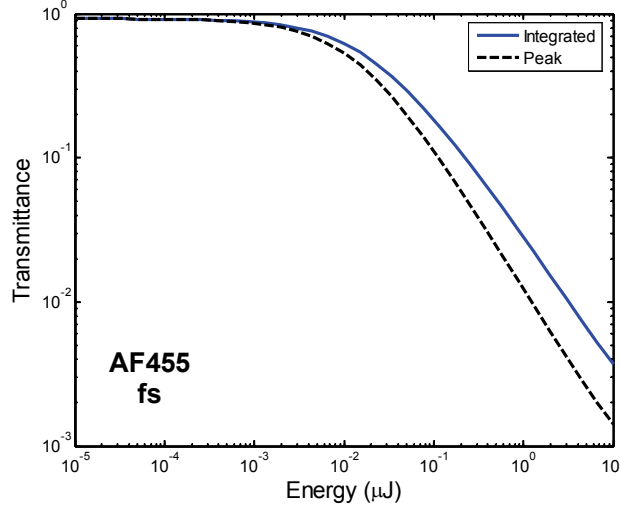


Fig. 8. Transmission as a function of input energy for AF455 in a 0.41 mm slab for femtosecond pulses; (solid line) using integrated value (dashed line) using peak values.

As stated previously our technique also enables us to examine the population dynamics and the contribution of each electronic level to the absorption. Fig. 9(a) illustrates the evolution of electron population densities at the sample entrance for an incident energy of  $6.6 \mu\text{J}$ . Because of the high energy of the pulse, the ground level is quickly depleted and does not repopulate due to slow decay rates  $k_{1,0}$  and  $k_{3,0}$ . We calculated its individual contributions to the total absorption, and their averaged values are  $\sim 95\%$  within the first part of pulse,  $\sim 48\%$  in the second part, and falls to less than  $10^{-2}\%$  at the final part. The depopulation of the ground level increases the electron density of the singlet-excited state  $N_1$  followed by fast excitation to  $N_3$ , so that in the second half of the pulse its individual contribution is  $\sim 51\%$ . However, as can be seen from the relative magnitudes of  $q_0$  and  $q_1$  in Fig. 9(b), the TPA is more important than ESA (to be more precise, the total absorption  $q$ , defined by Eq. (B3) (See Appendix B), averaged in the first part is  $\sim 0.22$ , whereas in the second part is  $\sim 0.08$ ), which makes AF455 mainly a TPA material in the fs regime as oppose to its TPA assisted ESA behavior in ns regime (refer to Table 3). Since the intersystem crossing time  $1/k_{1,3}$  is on the order of nanoseconds, the lowest triplet-triplet state  $N_3$  does not significantly contribute to the total absorption: its individual contribution is less than  $10^{-4}\%$  [therefore, we do not show it in Fig. 9(b)]. From our numerical calculation, we find that the maximum values of  $N_3$  and  $N_4$  are only about  $10^{-6}$ .

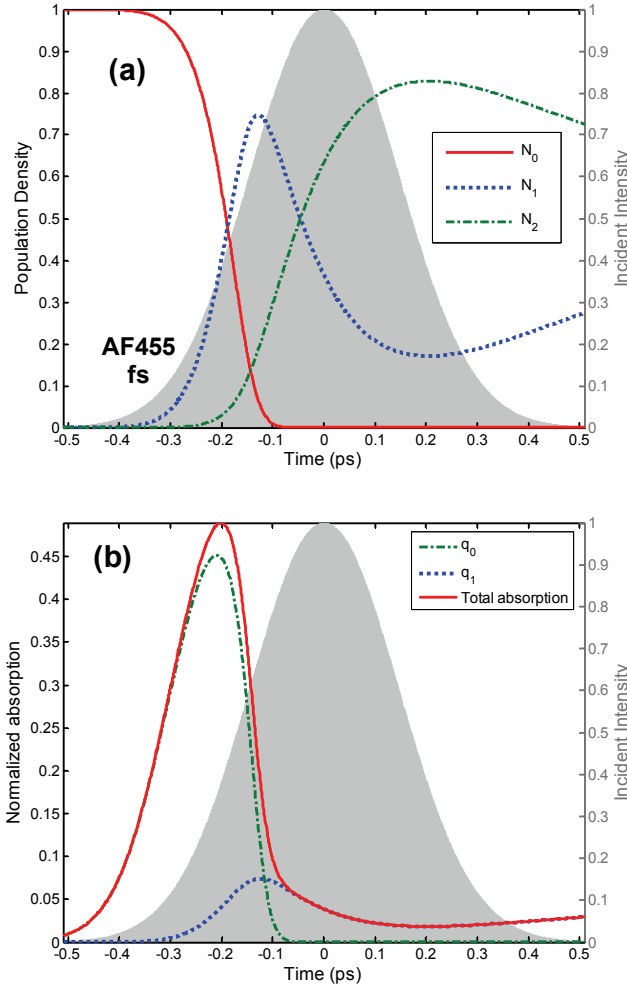


Fig. 9. AF455 femtosecond regime. (a) Evolution of population densities at the entrance of the 0.412 mm slab for 144.0 fs pulse at  $\rho = 0$ ; (b) contributions of active electron levels to the absorption superimposed with total intensity absorption.

### 3.3.2. Comparison with experiments on AF455

We demonstrated how a conventional five-level model of AF455 may be modified within our framework to a new six-level model, which enables better agreement with transmittance measurements at high input energies. Using experimental femtosecond transmission data on AF455 obtained from the Air Force Research Laboratory at Wright-Patterson AFB, we calculated transmittance of laser light with a wavelength of 780 nm and a pulse width of 175 fs through a sample of AF455, with molecular concentration  $N_0 = 1.85 \times 10^{18} \text{ cm}^{-3}$ , by solving the equations for the five-level model. Figure 10 shows a good fit of the five-level model to the measurements in the range from about 0.01  $\mu\text{J}$  to about 2  $\mu\text{J}$  using the following parameters<sup>31-32</sup>:  $\sigma_{12} = 1.68 \times 10^{-17} \text{ cm}^2$ ,  $\sigma_{34} = 17.1 \times 10^{-17} \text{ cm}^2$ ,  $\sigma_{TPA} = 0.51 \times 10^{-20} \text{ cm}^4/\text{GW}$ ,  $k_{10}^{-1} = 2.72 \text{ ns}$ ,  $k_{13}^{-1} = 45.3 \text{ ns}$ ,  $k_{21}^{-1} = 1.66 \text{ ps}$ ,  $k_{30}^{-1} = 368 \text{ ns}$ ,  $k_{43}^{-1} = 10 \text{ ns}$ . However, we can see from Fig. 10 (insert) that at energies exceeding 5  $\mu\text{J}$  the calculations diverge from the experimental data.

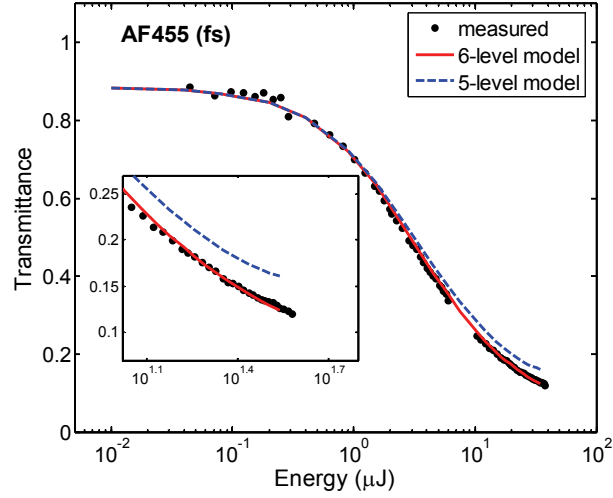


Fig.10. Experimental energy transmittance of TPA chromophore AF-455 (points) and calculated results for a new 6-level model (solid curve) versus 5-level model (dashed curve). 175fs ( $\text{sech}^2$  FWHM), 780nm, plane-polarized pulses from a Ti:S regenerative amplifier (Clark-MXR CPA-2010) were focused with either a 750mm or a 250mm lens into a 5.1mm thick PMMA slab doped with TPA chromophore AF-455 at a concentration of  $1.85 \times 10^{18} \text{ cm}^{-3}$ . The front face of the sample was positioned at the focal plane of the lens. The energy of the pulses was varied using a variable attenuator consisting of a rotatable waveplate and fixed polarizer. The range of input energies in this configuration was 0.04 to  $38.9 \mu\text{J}$ . Pulse energies were measured immediately before and after the sample and the ratio of transmitted to incident pulse energy computed. The inset image demonstrates the superiority of the 6-level model over the existing 5-level model within a range of high input intensities. Data are courtesy of the Air Force Research Laboratory.

We suggested adding a new sixth level as shown in Fig. 11 (5-level + 6-level). Then using the parameters  $k_{52}^{-1} = 160 \text{ fs}$  and  $\sigma_{25} = 0.78 \times 10^{-17} \text{ cm}^2$ , we achieved excellent agreement between the calculation and experiment.

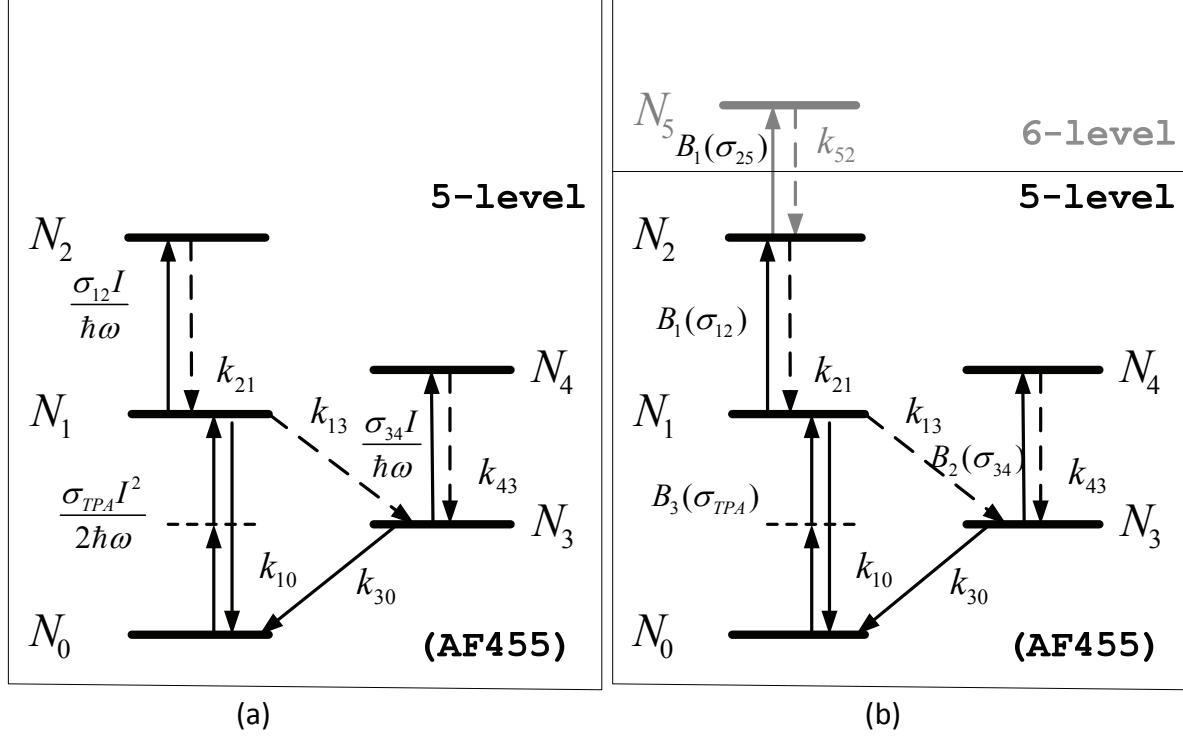


Fig.11. Extending an existing (5-level) model of AF455 to a new (6-level) model (a) Five-level Jablonski diagram. (b) Basic Block diagram extending an existing (5-level) model of AF455 to a new (6-level) model by introducing a new excited energy level within the singlet state group

Once a new hypothetical level has been introduced and tested by our technique, one can try to validate it by other techniques, such as z-scan or pump-probe measurements. We believe that adding new energy levels will be more and more important in the future when higher energy lasers become available.

### 3.4 General Numerical Method (Electric Field)

#### 3.4.1. Derivation of the theory

It is convenient to express the electric field in terms of a normalized function:

$$\tilde{E}(z, r, t) = \tilde{Q}(z, r, t)Q'_0, \quad Q_0^2 \equiv \epsilon_0 Q_0'^2. \quad (15)$$

Using the transformations provided above the electric field can be written in dimensionless parameters:

$$E(\eta, \rho, \tau) = Q(\eta, \rho, \tau)Q'_0. \quad (16)$$

To include diffraction effects in the model, the intensity is expressed in terms of a classical complex electric field,  $E_c$ , provided in Eq. (2), as follows:

$$\tilde{I} = \epsilon_0 n c_0 \langle E_c^2 \rangle \quad (17)$$

The system of equations can be made dimensionless using the transformations provided here together with the following relationship:

$$\langle E_c, E_c \rangle = 2Q_0'^2 \langle Q, Q \rangle = \frac{2}{\varepsilon_0} Q_0^2 \langle Q, Q \rangle, \quad (18)$$

which leads to the following expression for the field intensity:

$$\tilde{I}(\eta, \rho, \tau) = 2nc_0 Q_0^2 \langle Q(\eta, \rho, \tau), Q(\eta, \rho, \tau) \rangle \equiv 2nc_0 Q_0^2 \bar{Q}(\eta, \rho, \tau), \quad (19)$$

with

$$\bar{Q} \equiv \langle Q, Q \rangle. \quad (20)$$

Using the transformations described above, the rate equation becomes:

$$\frac{d\mathbf{N}(\eta, \rho, \tau)}{d\tau} = T_0 \left[ \hat{D}_0 + \sum_{\alpha=1}^{N_A} \frac{\hat{D}_\alpha}{\alpha \hbar \omega_0} (2nc_0 Q_0^2)^\alpha \bar{Q}^\alpha(\eta, \rho, \tau) \right] \mathbf{N}(\eta, \rho, \tau). \quad (21)$$

Eq. (21) can be expressed in a more compact form by using the following substitutions:

$$D_0 \equiv T_0 \hat{D}_0, \quad D_\alpha \equiv T_0 \frac{\hat{D}_\alpha}{\alpha \hbar \omega_0} (2nc_0 Q_0^2)^\alpha. \quad (22)$$

which leads to the following rate equation:

$$\frac{d\mathbf{N}(\eta, \rho, \tau)}{d\tau} = \left[ D_0 + \sum_{\alpha=1}^{N_A} D_\alpha \bar{Q}^\alpha(\eta, \rho, \tau) \right] \mathbf{N}(\eta, \rho, \tau), \quad (23)$$

### 3.4.2 Description of the rate and propagation operators

A rate operator  $\Upsilon$  is introduced as

$$\Upsilon(\eta, \tau) \equiv \Upsilon_0 + \sum_{\alpha=1}^{N_A} \Upsilon_\alpha^{\bar{Q}}(\eta, \tau), \quad (24)$$

with  $\Upsilon_0 \equiv D_0$  and  $\Upsilon_\alpha^{\bar{Q}}(\eta, \tau) \equiv D_\alpha \bar{Q}^\alpha(\eta, \rho, \tau)$ . This leads to the following compact form of the rate equation:

$$\frac{d\mathbf{N}(\eta, \rho, \tau)}{d\tau} = \Upsilon(\eta, \tau) \circ \mathbf{N}(\eta, \rho, \tau), \quad (25)$$

Using the transformation provided in Eq. (19), a dimensionless propagation equation, which does not contain a term to account for diffraction effects can be written as:

$$\frac{dQ(\eta, \rho, \tau)}{d\eta} = \left\{ -L_{df} N \left[ \sum_{\beta=1}^{N_B} (\tilde{\boldsymbol{\sigma}}_\beta \cdot \mathbf{N}(\eta, \rho, \tau)) (2nc_0 Q_0^2)^{\beta-1} \bar{Q}^{\beta-1}(\eta, \rho, \tau) \right] - \tilde{c} L_{df} \right\} Q(\eta, \rho, \tau), \quad (26)$$

or, equivalently, as:

$$\frac{dQ(\eta, \rho, \tau)}{d\eta} = \left\{ -\sum_{\beta=1}^{N_B} (\boldsymbol{\sigma}_\beta \cdot \mathbf{N}(\eta, \rho, \tau)) \bar{Q}^{\beta-1}(\eta, \rho, \tau) - c \right\} Q(\eta, \rho, \tau), \quad (27)$$

by using the substitutions  $\sigma_\beta \equiv L_{df} N (2nc_0 Q_0^2)^{\beta-1} \tilde{\sigma}_\beta$  and  $c \equiv \tilde{c} L_{df}$ . Eq. (27) can be rewritten in an operator form by introducing absorption operators  $\Phi_\beta^Q$ ,  $\Phi_\beta^N$ , and  $\Phi_L$  to account for absorption due to the intensity, electronic density, and the linear absorptions, respectively, where  $\Phi_\beta^N(\eta, \tau) \equiv \sigma_\beta \cdot \mathbf{N}(\eta, \rho, \tau)$ ,  $\Phi_\beta^Q(\eta, \tau) \equiv \bar{Q}^{\beta-1}(\eta, \rho, \tau)$ , and  $\Phi_L \equiv c$ . The resulting equations can be expressed as:

$$\Phi(\eta, \tau) \equiv -\sum_{\beta=1}^{N_B} (\sigma_\beta \cdot \mathbf{N}(\eta, \rho, \tau)) \bar{Q}^{\beta-1}(\eta, \rho, \tau) - c = -\sum_{\beta=1}^{N_B} \Phi_\beta^N(\eta, \tau) \Phi_\beta^Q(\eta, \tau) - \Phi_L, \quad (28)$$

and

$$\frac{dQ(\eta, \rho, \tau)}{d\eta} = \Phi(\eta, \tau) \circ Q(\eta, \rho, \tau). \quad (29)$$

An absorption operator that accounts for diffraction effects (e.g., a diffraction operator) can be written as:

$$\Psi_{df}(\rho, \tau) \equiv \frac{i}{4} \left( 1 - ib \frac{\partial}{\partial \tau} \right) \nabla_\rho^2, \quad (30)$$

with

$$b \equiv \frac{1}{\omega_0 T_0}. \quad (31)$$

A Fourier transform of this operator has the following form:

$$\Psi_{df}(\rho, \omega) \equiv \frac{i}{4} (1 - b\omega) \nabla_\rho^2, \quad \tilde{F} \left( \frac{\partial^n}{\partial \omega^n} \right) \equiv (-i\omega)^n. \quad (32)$$

By adding together the nonlinear and linear absorption terms, the propagation equation can be expressed in terms of the electric field as:

$$\frac{dQ(\eta, \rho, \tau)}{d\eta} = \{ \Phi(\eta, \tau) + \Psi(\rho, \tau) \} \circ Q(\eta, \rho, \tau). \quad (33)$$

This propagation equation includes complex values of  $Q(\eta, \rho, \tau)$ , whereas the rate equation provided in Eq. (25) can be expressed in terms of real vectors  $\mathbf{N}(\eta, \rho, \tau)$  and real values of  $\bar{Q}(\eta, \rho, \tau)$ .

### 3.5 Relationship between the Building Blocks/decay rates and the Coupled Propagation/Rate Equations

A detailed description for a more general set of building blocks is provided by describing associated schematic energy diagrams, descriptive notations, and a technique for building a coupled system of rate-propagation equations based on an energy diagram descriptor,  $\chi_{\text{material}}$ , which is expressed in terms of individual building blocks.. Two types of computational building blocks is used to describe generic materials: absorption blocks and inverse absorption blocks. The absorption blocks are associated with transitions from a lower energy level to a higher one, whereas the inverse absorption blocks are associated with transitions from a higher energy level to a lower one. Such building blocks are used to describe energy level diagrams associated with



a variety of photoactivated materials. They can also be used to uniquely define terms in a corresponding coupled system of rate-propagation equations which can describe interactions between, e.g., electromagnetic pulses and absorbing materials.

### 3.5.1. Energy Level Diagrams and Computational Building Blocks

An energy level diagram can be used to develop a set of computational building blocks. Energy levels can be associated with electronic states, vibrational and/or rotational electronic substates in atoms, molecules and solids, and/or bands and discrete levels in semiconductors and metals. An energy level diagram can also define possible electron and/or exciton transitions between such energy levels by describing transitions and corresponding absorption cross-sections or decay time values. An energy level diagram may be constructed using quantum calculations, e.g., calculations based on Schrödinger equations, experimental measurements, and/or hypothetical formulations constructing a proposed diagram or adding elements to an existing diagram.

The Schrödinger equation can include all possible energy levels and/or states that a material system can be in at a particular moment in time and a particular place in space, and can describe the evolution of such material system. For example, a particle of mass  $M$  (e.g., an electron) having a potential energy  $V_p(\vec{r}, t)$  can be described by a wavefunction  $\Psi_{SE}(\vec{r}, t)$  that satisfies the following Schrödinger equation:

$$-\frac{\hbar^2}{2M} \nabla^2 \Psi_{SE}(\vec{r}, t) + V_p(\vec{r}, t) \Psi_{SE}(\vec{r}, t) = i\hbar \frac{\partial \Psi_{SE}(\vec{r}, t)}{\partial t}. \quad (34)$$

Systems containing many particles, e.g., atoms, molecules, liquids or solids, can be described using more complex but similar equations as described in Ref. 46. The probability of locating a particle within a volume  $d\nu$  about the position  $\vec{r}$  in a time interval between  $t$  and  $t + dt$  can be written as:

$$P(\vec{r}, t) d\nu dt = |\Psi_{SE}(\vec{r}, t)|^2 d\nu dt. \quad (35)$$

Allowable energy levels  $E^n$  of the particle can be obtained by neglecting time-varying interactions, using the following form of a wavefunction, expressed as a product of spatial and temporal terms:

$$\Psi_{SE}(\vec{r}, t) = \psi(\vec{r}) \exp[i(E^n / \hbar)t], \quad (36)$$

The spatial term  $\psi(\vec{r})$  can be described by the following time-independent Schrödinger equation:

$$-\frac{\hbar^2}{2M} \nabla^2 \psi(\vec{r}) + V_p(\vec{r}) \psi(\vec{r}) = E^n \psi(\vec{r}), \quad (37)$$

and the energy levels  $E^n$  can be determined as eigenvalues of the operator equation

$$\hat{H} \psi(\vec{r}) = E^n \psi(\vec{r}), \quad (38)$$

where the operator  $\hat{H}$  can be obtained from Eq. (37) as

$$\hat{H} = -\frac{\hbar^2}{2M} \nabla^2 + V_p(\vec{r}). \quad (39)$$

The size of the energy level diagram containing most or all possible energy levels may be infinite, so that a reasonable simplification should be used to limit the number of levels contained there. For example, the size of an energy level diagram can be reduced by including only such energy levels which may be important in describing the evolution of a particular system (or which may contribute the most to a particular physical phenomenon of interest), and/or those which may be revealed or explained by experimental measurements. Conventional energy level diagrams may be constructed in this way, and can provide an appropriate agreement between mathematical models based on such diagrams and experimental observations.

Certain materials can exhibit measured characteristics and/or behavior (e.g., optical transmittance) which may not fully agree with the existing model that can be limited to a particular set of energy levels. For example, additional energy levels may need to be added to an existing model as new experimental techniques and/or conditions are provided such as a new laser frequency, a higher laser intensity obtained using a reduced temporal pulse width, etc. Such further hypothetical energy level diagrams can be provided based on experience, judgment and/or comparisons with energy diagrams of similar materials. A mathematical model based on a new energy level diagram can be tested against the experimental measurements. An example of this approach is  $C_{60}$ , which was originally described using an energy diagram having only low-lying singlet states to explain experimental absorption data. However, later experiments did not agree with this simple model, and an additional set of triplet states was added to the energy level diagram. Determinations based on this additional energy level diagram exhibited a better agreement with the experimental measurements.

The energy levels can be obtained as eigenvalues of the Schrödinger time-independent operator equation provided in Eq. (38). There can be an infinite number of discrete energy levels (e.g., electronic levels of an isolated atom) associated with a material based on a solution to this equation. The materials that include many atoms (e. g., molecules or crystals) can have additional energy levels associated with a certain electronic energy level. To simplify construction of an energy level diagram, a set of energy levels provided by the Schrödinger equation can be restricted to those levels required to generate reasonable agreement between calculations and experimental measurements.

### 3.5.2 Energy Level Diagrams

For example, Figs. 12 (a)-(c) show energy levels which can be used in energy level diagrams. A certain vibrational and/or rotational energy levels associated with it which may be degenerate with respect to an energy level as shown in Fig.12(b). The electronic energy level can have vibrational levels associated therewith, and rotational levels can degenerate with respect to these vibrational levels, as shown in Fig.12(c). Details of the vibrational energy levels  $v^i$  and rotational energy levels  $u_j^i$  are shown in Fig.12(c). There may be a small difference between the vibrational and rotational energy levels as compared to an energy difference between various electronic levels. The vibrational and rotational energy levels can be referred to as “sub-levels” or as a “manifold of states” associated with a particular electronic energy level or “state.”

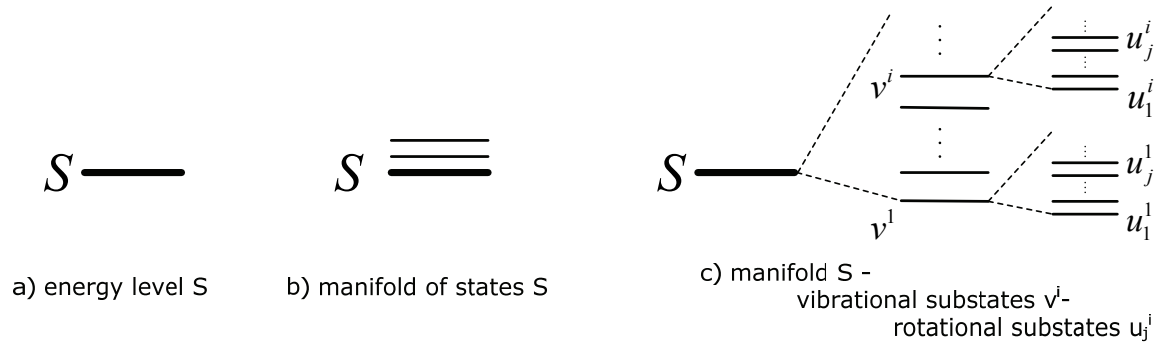


Fig.12. Energy level diagrams. (a) single electronic level, (b) manifold of states, (c) vibrational and rotational states.

A small, finite set of energy levels may be used to describe certain energy level diagrams. The term “*energy level*” can represent either an energy level  $E^n$  obtained as an eigenvalue of the operator equation provided in Eq.(38), or a degenerate energy level as shown in Fig.12. An energy level can be included in an energy level diagram, if such energy level provides a significant contribution to a macroscopically observable physical phenomenon such as an experimental measurement or a known absorption mechanism.

In many systems that include an absorbing material interacting with a laser operating in the UV to near IR spectral regions, the vibrational and/or rotational energy sublevels within a manifold of states may exhibit very short life times compared to a temporal pulse width of the laser. In such systems, electrons from higher energy substates can relax to a lowest possible substate within a manifold in a time that is much shorter than the duration of a pulse, so that the contributions of these higher energy substates to a macroscopic physical phenomenon may be ignored.

### 3.5.3. Energy Level Criteria

The following criteria are used to select and/or build energy levels associated with particular materials to form an energy level diagram:

1. levels that are reachable and/or accessible by entities energetically promoted by one or more incident photons;
2. levels that can provide a significant contribution to a macroscopic physical phenomenon, such as one indicated or suggested by experimental measurements;
3. levels which can be degenerate energy levels or combinations of degenerate levels; and
4. levels provided based on theoretical predictions.

According to the first criterion above, energy levels may be selected, which can be reached and/or accessed by entities (e.g., electrons or excitons) that may absorb incident photons. The second criterion can allow a selection, from the energy levels which may satisfy the first criterion, of a smaller number of energy levels which, when using a mathematical model, may be used to describe and/or account for macroscopic phenomena such as measured physical absorption processes. The third criterion can allow combination of certain energy levels to form degenerate energy levels by a combination of vibrational and/or rotational sublevels within a

particular manifold of electronic states. The third criterion can also allow a combination of such degenerate levels into a further “joint” degenerate energy level. The fourth criterion can allow the building blocks to be used to expand conventional energy level diagrams or to build new energy level diagrams by introducing additional levels. This procedure can provide a more accurate description of absorption phenomena in a particular material without requiring a new algorithm or numerical method to solve a set of equations describing the expanded energy level diagram for the material. For example, when using the lasers having greater intensity and/or spectral ranges, additional terms may be added to an existing energy level diagram for a particular material to achieve consistency between the predictions and the experimental measurements.

### 3.5.4 Absorption/Reverse Absorption Block

An absorption block from the set B<sub>0</sub>-B<sub>5</sub> represents a mechanism that includes simultaneous absorption of  $\alpha$  photons by an entity (e.g., an electron or an exciton) and dislocation of an entity (e.g., an electron or an exciton) from a particular energy level  $N_{s_1}$  to another energy level  $N_{s_2}$ . We distinguish two types of photon absorption mechanisms in this framework: a forward absorption, for which  $\alpha > 0$ , refers to an absorption mechanism in which a photoactivated entity (e.g., an electron or an exciton) is promoted from a lower energy level to a higher energy level, and a reverse absorption which refers to an absorption mechanism in which an electron relaxes from a higher energy level to a lower energy level by re-emitting one or more photons that is coherent with the incident light. This mechanism, for which  $\alpha < 0$ , describes the phenomenon of stimulated emission.

For example, an absorption block diagram shown in Fig.13 includes indices  $s_1, s_2$  which may represent certain energy levels that an electron is promoted “from” and “to” respectively (or relaxed “to” and “from” respectively if  $\alpha < 0$ ). The parameter  $\alpha$  represents the number of photons that is absorbed to promote an electron from level  $s_1$  to level  $s_2$ , where  $\alpha$  can be negative if the expression is used to represent a reverse absorption block that includes a relaxation from level  $s_2$  to level  $s_1$ . Optionally, the parameter  $\alpha$  may be omitted if it is equal to one.

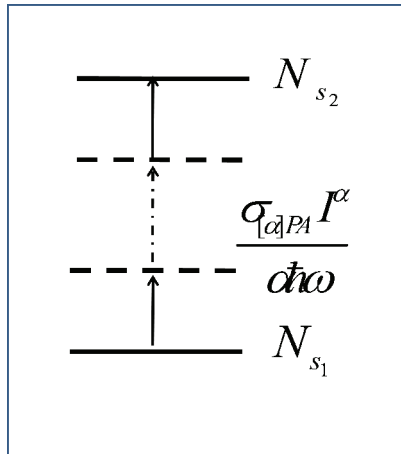


Fig. 13. Energy level diagram for absorption of  $\alpha$ -photons.

### 3.5.5. Example of absorption block descriptor

The energy diagram for AF455 can be represented as the following energy level diagram descriptor, using the computational building block notation described here:

$$\chi_{AF455} = \{B_1, B_2, B_3\} \quad (40)$$

where,  $B_3$  represents a simultaneous absorption of two photons and promotion of one electron from a ground level to a lowest excited level of the singlet state;  $B_2$  represents an absorption of one photon and promotion of one electron from the lowest excited state to the higher excited state in the triplet state;  $B_1$  represents an absorption of one photon and promotion of one electron from the first excited state to the higher excited state in the singlet state.

### 3.5.6. Stimulated emission

An example of stimulated emission can be described from a two-photon absorption (TPA) state with nonlinear excited-state absorption (ESA). The emission may be to a conduction band or it may be a free electron excitation. A material that can exhibit stimulated emission effects and which may be described is a Green Fluorescent Protein (GFP) <sup>47</sup>

For example, an electronic configuration of a material is shown in the figure below which includes certain states: a ground state manifold  $N_0$ , a first excited state manifold  $N_1$ , which may be reached through a TPA event and can be referred to as a TPA-state, and a second excited state  $N_2$ , which can be reached via a one photon absorption event from the first excited state manifold. The second excited state can be referred to as a ESA-state, and it may be a conduction band or a free electron excitation. A stimulated emission can occur between the first excited state and the ground state. A spontaneous emission can occurs between the second excited state and the first excited state, or between the second excited state and the ground state.

(a)

(b)

Fig. 14. Green Fluorescent Protein: (a) Jablonski diagram of TPA and ESA. (b) Building Block diagram showing stimulated emission and decay rates.

Parameters  $k_{10}$  and  $k_{21}$  shown in Fig. 14 can represent decay rates of the TPA-state and the ESA-state, respectively, and the parameter  $k_{20}$  can represent a decay rate from second excited state 1 to the ground state. The corresponding matrices that may be used in the rate equation can be written as:

$$\hat{D}_0 = \begin{bmatrix} 0 & k_{10} & k_{20} \\ 0 & -k_{10} & k_{21} \\ 0 & 0 & -(k_{20} + k_{21}) \end{bmatrix}; \quad \hat{D}_1 = \begin{bmatrix} 0 & 0 & 0 \\ 0 & -\sigma_{ESA} & 0 \\ 0 & \sigma_{ESA} & 0 \end{bmatrix};$$

$$\hat{D}_2 = \begin{pmatrix} -g^{10}\sigma_{TPA} & \sigma_{TPA} & 0 \\ g^{10}\sigma_{TPA} & -\sigma_{TPA} & 0 \\ 0 & 0 & 0 \end{pmatrix}. \quad (41)$$

The parameter  $g^{10} = g^1 / g^0$  may also be used, where  $g^1$  and  $g^0$  can represent an electron degeneracy of electronic levels 1 and 0, respectively. In the present example, all other matrices:  $\hat{D}_{N_A}(\sigma_{[N_A]PA}) = 0$ ;  $\sigma_1 = (0, \sigma_{ESA}, 0)$ ,  $\sigma_2 = (g^{10}\sigma_{TPA}, \sigma_{TPA}, 0)$ ; and all other vectors  $\sigma_{N_B}(\sigma_{[N_B]PA}) = 0$ .

### 3.5.7. Absorption blocks and decay rates

Each absorption building block and corresponding relaxation rate matrix can define a unique corresponding term in the coupled system of rate-propagation equations provided in Eqs. (A5) and (A6), which may be used to describe propagation of an electric field through a sample of a photoactive material. The computational building blocks described here are analogous or similar to computational molecules that are used to formulate multidimensional finite difference numerical schemes.

A particular energy diagram descriptor  $\chi_{mat}$  associated with a photoactivated material  $mat$  can include a component  $b \in \chi_{mat}$ . The component  $b$  can represent one of the types of the absorption building block or the stimulated emission building block. Each computational building block can provide certain terms in a matrix  $\hat{D}_\alpha$ ,  $\alpha > 0$ , and a vector  $\sigma_\beta$  which appear in the rate and propagation equations provided in Eqs. (A5) and (A6).

#### 3.5.7.1 Representation of absorption block/decay rate parameters

For example,  $b$  can represent an absorption building block, B<sub>0</sub>-B<sub>7</sub>, which may be associated with an absorption parameter  $\sigma_{s_1 s_2}^{\pm 1}$ ,  $\sigma_{[\alpha]PA}$ , or  $\sigma_{[\alpha]PA}^{(-\alpha)}$ , where  $s_1$  and  $s_2$  are described above and

$\alpha > 0$ . The value of this parameter can be included at corresponding places in the matrix  $\hat{D}_\alpha$  and vector  $\sigma_\beta$ , which can lead to the following expressions:

For  $\alpha = 1$  and  $\sigma_{s_1 s_2}$ , the expressions are given by

$$\hat{D}_1[s_1, s_1] = \hat{D}_1[s_1, s_1] - \sigma_{s_1 s_2} \quad (42)$$

$$\hat{D}_1[s_2, s_1] = \hat{D}_1[s_2, s_1] + \sigma_{s_1 s_2}, \quad (43)$$

and

$$\sigma_1[s_1] = \sigma_1[s_1] + \sigma_{s_1 s_2}. \quad (44)$$

For  $\alpha = 1$  and  $\sigma_{s_1 s_2}^{(-1)}$ , the expressions are given by

$$\hat{D}_1[s_2, s_2] = \hat{D}_1[s_2, s_2] - \sigma_{s_1 s_2}^{(-1)} \quad (45)$$

$$\hat{D}_1[s_1, s_2] = \hat{D}_1[s_1, s_2] + \sigma_{s_1 s_2}^{(-1)}, \quad (46)$$

and

$$\sigma_1[s_1] = \sigma_1[s_1] - \sigma_{s_1 s_2}^{(-1)}. \quad (47)$$

For  $\alpha > 1$  and  $\sigma_{[\alpha]PA}$ , when an absorption transition involves states  $s_1$  and  $s_2$ , the expressions are given by

$$\hat{D}_\alpha[s_1, s_1] = \hat{D}_\alpha[s_1, s_1] - \sigma_{[\alpha]PA} \quad (48)$$

$$\hat{D}_\alpha[s_2, s_1] = \hat{D}_\alpha[s_2, s_1] + \sigma_{[\alpha]PA} \quad (49)$$

and

$$\sigma_\alpha[s_1] = \sigma_\alpha[s_1] + \sigma_{[\alpha]PA} \quad (50)$$

For  $\alpha > 1$  and  $\sigma_{[\alpha]PA}^{(-\alpha)}$ , when an absorption transition involves states  $s_2$  and  $s_1$ , the expressions are given by

$$\hat{D}_\alpha[s_2, s_2] = \hat{D}_\alpha[s_2, s_2] - \sigma_{[\alpha]PA}^{(-\alpha)} \quad (51)$$

$$\hat{D}_\alpha[s_1, s_2] = \hat{D}_\alpha[s_1, s_2] + \sigma_{[\alpha]PA}^{(-\alpha)} \quad (52)$$

and

$$\sigma_\alpha[s_1] = \sigma_\alpha[s_1] - \sigma_{[\alpha]PA}^{(-\alpha)} \quad (53)$$

The various decay rates for each transition can be placed in the matrix  $\hat{D}_0$  according to Eq. (9).

### 2.5.7.2. Examples of inclusion of parameters in matrices and vector

The matrices  $\hat{D}_0$ ,  $\hat{D}_\alpha$  and the vector  $\sigma_\beta$  which appear in the rate and propagation equations provided in Eqs. (A5) and (A6) may be constructed for a particular material using the following procedure. For example, each matrix  $\hat{D}_0$ ,  $\hat{D}_\alpha$  and the vector  $\sigma_\beta$  may be defined initially to

have all elements equal to zero. The energy diagram descriptor  $\chi_{mat}$ , for a given photoactive material can be obtained using the procedures described here. Each computational building block/decay rate appearing in  $\chi_{mat}$  can then be used to modify certain elements in the matrices  $\hat{D}_0$ ,  $\hat{D}_\alpha$  and the vector  $\sigma_\beta$ . For example, for  $\alpha=1$  and  $\sigma_{s_1s_2}$ , Eqs.(42)-(44) or, for  $\alpha=1$  and  $\sigma_{s_1s_2}^{(-1)}$ , Eqs. (45)-(47) can be applied for each absorption block that appears in the energy diagram descriptor. As another example, for  $\alpha>1$  and  $\sigma_{[\alpha]PA}$ , Eqs. (48)-(50) or, for  $\alpha>1$  and  $\sigma_{[\alpha]PA}^{(-\alpha)}$ , Eqs. (51)-(53) can be applied for each absorption block that appears in the energy diagram descriptor. This procedure can be repeated until all component  $b$  in the energy diagram descriptor (e.g., all absorption coefficients and decay rates) have been used to modify appropriate elements in the matrices  $\hat{D}_0$ ,  $\hat{D}_\alpha$  and the vector  $\sigma_\beta$  using Eqs. (42)-(53). The resulting matrices and vector may be provided in Eqs. (A5) and (A6), and these equations may be solved using procedures described here to determine the absorption behavior of the particular material.

### 3.6 Semiconductor Quantum Dots

#### 3.6.1 Fabrication Techniques

Semiconductor quantum dots (QDs) are often referred to as artificial atoms (See figure below), which consist of hundreds to thousands of atoms. A few reviews of the synthesis, structure and properties of nanomaterials are given the references 48-50. In the 1980s researchers formulated the concept of size quantization<sup>51-53</sup> which was later expanded<sup>54,55</sup>. As a result of the quantum confinement, QDs exhibit unique physical and optical properties that are not present in bulk material. The terminology used for QDs evolved over several years and is reviewed in ref. 56. A material is denoted as a QD if the size of the material is smaller than the Bohr radius i.e. the size of material is less than the extension of the electron-hole pair in bulk material. In this case, an exciton formed in the QD has no degrees of freedom and no motion is possible for the exciton.

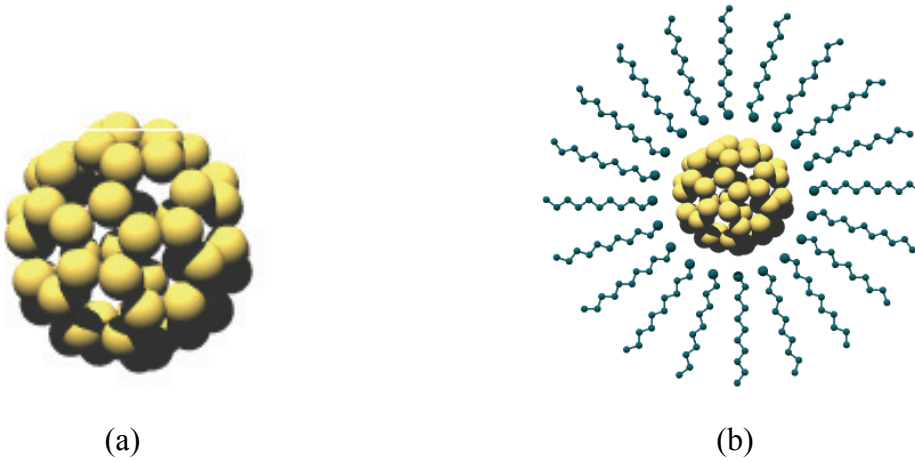




Fig. 15. Schematic diagrams of a semiconductor quantum dot (QD): (a) QD alone where each atom is represented by the gold sphere; (b) core/shell structure (QD with organic shell which is represented by the blue lines).

### 3.6.1.1 Methods of colloidal synthesis

There are common methods for chemical synthesis of QDs: (1) Arrested precipitation using a stabilizing agent. (2) Reverse micelles. An example of the first method<sup>57</sup> is given by the formation of CdS QDs in which a Cd cupferronate solution in toluene is poured on the surface of Na<sub>2</sub>S aqueous solution to form QDs at the interface. The QD size is controlled by varying the reagent concentrations, temperature and reaction duration. A common stabilizer for the reaction is tri-octylphosphine oxide (TOPO). An example of the second method<sup>58</sup> is given as follows: CdS QDs are formed by preparing two mixtures, water-toluene and water-surfactant. One aqueous phase contains the required amounts of a Cd salt; while, the other one contains sodium sulfide. Mixing these two solutions results in micelle capped QDs as shown in part (b) of the above figure.

### 3.6.1.2 Core-shell quantum dots

The surface to volume ratio in QDs plays a significant role. A review of surface properties is given in ref. 59. In order to passivate the QD surface, other materials are used forming a so-called core-shell QD. Inorganic shells are often fabricated from another semiconductor which differs from the core material. Common examples of semiconductor-semiconductor core-shell QDs are CdS/CdSe and CdSe/ZnS. A common synthesis comprises a shell buildup by deposition of cations and anions on the surface of QDs by successive ion layer adsorption and reaction<sup>60</sup>. A semiconductor-semiconductor core-shell QD can be thought of as a solid solution of two chalcogenides; typically, these materials have higher efficiency of photoluminescence. The reverse micelles also form a core-shell structure, but their photoluminescence properties have not been studied in as much detail as the semiconductor-semiconductor core-shell QDs.

### 3.6.1.3 Quantum dot nanostructures

#### 3.6.1.3.1 Quantum dots on substrates

In many applications a planar structure is needed as in photo-electronic or electronic devices. Methods include molecular epitaxy and metal organic chemical vapor deposition, which are well known in semiconductor laboratories<sup>61</sup>. Chemical methods can also be used such as self-assembled on a surface. A monolayer of CdS QDs on a substrate was performed by fabricating reverse micelles stabilized with sodium bis(2-ethylhexyl)sulfosuccinate<sup>62</sup>. Additional treatment with dithiol created a multilayer structure for the QDs<sup>63</sup>. Layer-by-layer adsorption techniques<sup>64</sup> have also been used to create organized QD structures.

#### 3.6.1.3.2 Quantum dots in inorganic matrices

The small size of the inner cavities of zeolites allows for the synthesis of QDs. An example of this method for CdS and PbS was investigated in ref. 65. In this case the QD size was restricted to 1 nm. Another method involves mesoporous silica gel<sup>66</sup> as a matrix for QD. An example is given by CdS QDs bonded to Zn atoms of Zn-doped material through dithiol bridges<sup>67</sup>. These structures yield a high photocatalytic activity.

### 3.6.1.3.3 Quantum dots in polymers

QD in polymers is a very active field. An example is given by modifying CdS QDs<sup>68</sup> on the surface of SiO<sub>2</sub> nanogranules by using a radical polymerization initiator followed by polymerization of the methyl methacrylate. The polymer solution with the QDs was poured on the substrate and the solvent was removed. Researchers believe that high photoluminescence can be achieved with QDs well distributed in a polymer matrix.<sup>69</sup>

### 3.6.2. Electronic levels of quantum dots

A quantum dot (QD) is a quasi-zero-dimensional object where the carrier movement is restricted in three dimensions. The bulk crystalline structure of the semiconductor is maintained in the QD, but they have atomic-like discrete energy states due to 3D confinement.<sup>70</sup>

(a)

(b)

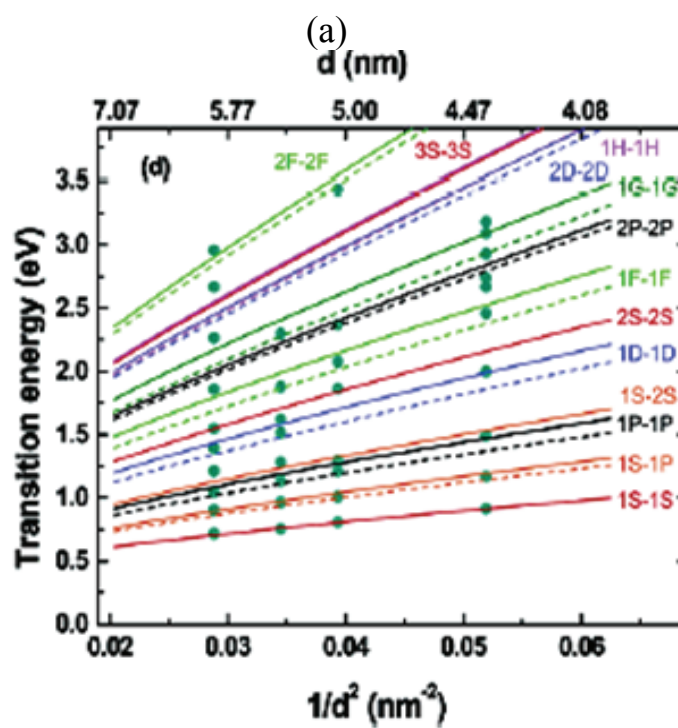
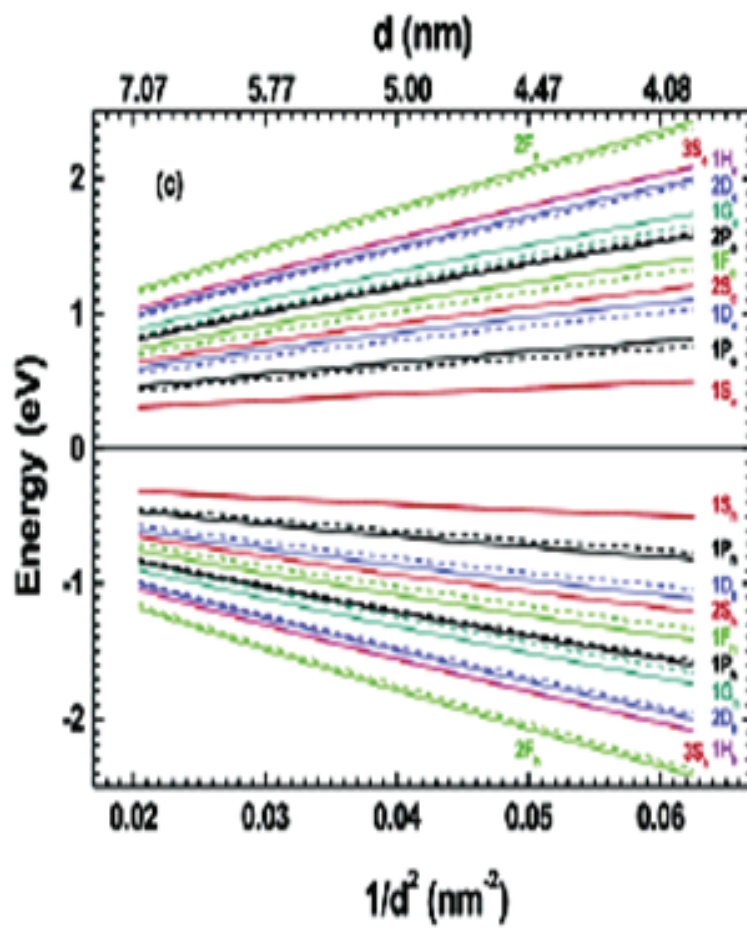
Fig. 16. Energy level diagrams. (a) bulk semiconductor (b) quantum dot assuming single valence bands.

Carrier dynamics in QDs are quite different from bulk materials due to the large energy level spacing and enhanced surface-to-volume ratio. State-filling is the main mechanism for optical nonlinearities.<sup>71-72</sup> Typically the effective-mass model is used to describe the electronic structure of QDs<sup>73</sup>. In this description, electron states are annotated by using a letter ( $l$ ) to denote the angular momentum of the envelop wave functions. Using spectroscopic notation, the following symbols are used S for  $l=0$ , P for  $l=1$ , D for  $l=2$ , etc. The degeneracy of the electron states are  $2(2l+1)$ -fold degenerate and the lowest three electron states are denoted by 1S, 1P, 1D. The hole states are generally more complicated than shown in the figure above and are labeled similarly to electron states with an additional subscript for the total hole angular momentum ( $j$ ), which have

a degeneracy of  $2j + 1$ . The first three hole states are  $1S_{3/2}, 1P_{3/2}, 2S_{3/2}$ . The interband selection rules allow for transitions from  $nS_j(h)$  hole states to all  $S(e)$  electron states,  $nP_j(h)$  hole states to all  $P(e)$  electron states, etc. where  $n$  is the ordinal number of the level. A schematic diagram is given in the figure below.

Fig. 17. Energy level diagram and transitions for semiconductor quantum dot.

The above figure shows five absorptive transitions of a single photon from states  $1S_{3/2}$  to  $2S$ ;  $2S_{3/2}$  to  $2S$ ;  $1P_{3/2}$  to  $1P$ ;  $1P_{1/2}$  to  $1P$  and  $1S_{1/2}$  to  $1P$ . The energies of the excitons depend on the relative energies of the electron and hole states. The energies of the exciton transitions may be obtained from spectroscopic measurements. Often these spectroscopic measurements are compared to theoretical calculations of the electron and hole energy levels. The figure below shows the theoretical calculations for PbSe QDs.<sup>74</sup> Part (a) of the figure shows the theoretical electron and hole energy levels as a function of QD size; while, part (b) shows the theoretical exciton energy states from part (a) following transition rules and electron degeneracy as described above.



(a)

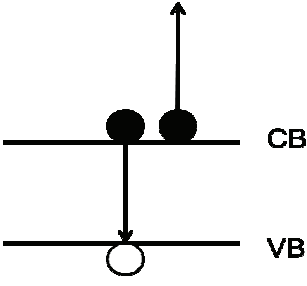
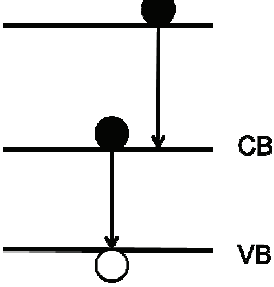
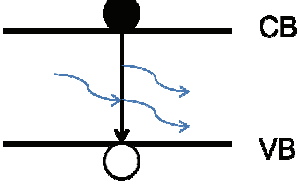
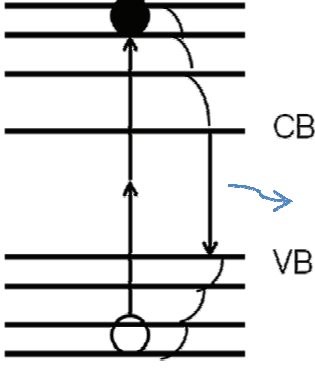
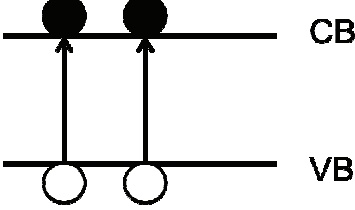
Fig.18. Electronic levels for PbSe QDs. (a) Theoretical energy levels as a function of QD size. (b) Theoretical transitions for four QD sizes with experimental transitions shown as dots. (Revised figure from Ref. 74.)

### 3.6.3. Generation and recombination of excitons

There are several generation/recombination processes in semiconductors<sup>76-80</sup>. The table below describes the major processes. A particular process known as the Auger process is non-radiative and is mediated by electron-electron (e-e) Coulomb interactions, which differ amongst atoms, bulk semiconductors and QDs. In atomic systems the e-e coupling is much stronger than the electron-phonon coupling which makes the rates of Auger transitions much greater than the radiative transitions. Thus the decay of multi-electron levels is dominated by Auger processes. However, in bulk semiconductors the efficiency of the Auger process is reduced because the e-e interactions are smaller. The situation in QDs differs from the bulk in that the quantum confinement enhances the e-e leading to increased Auger rates. Additionally, QDs have a large surface to volume ratio that leads to trap states in the band gap (not shown in the table). In many QDs the surface states are passivated by capping the QD.

Table 4. Type, description and schematic diagram of various recombination mechanisms of excitons<sup>76-80</sup>.

Diagram	
<b>Band-to-band: single electron decay or absorption</b>  Generation or recombination: Electron decay (shown on right) or absorption from its state in the conduction or valence band and occupies or creates the hole in the valence band: $E_{\text{photon}} > E_{\text{gap}}$	
<b>Trap-assisted</b>  Electron and hole combine in a trap state in the band gap	

<p><b>Auger</b></p> <p>Electron and hole combine in a band-to-band transition and the energy is absorbed by another electron in the conduction band or a hole in the valence band</p>	
<p><b>Impact ionization</b></p> <p>Generation mechanism that is the counterpart to Auger recombination. Occurs when an electron has energy much larger than the conduction band edge. The excess energy is generates an electron-hole pair through band-to-band transition.</p>	
<p><b>Stimulated emission</b></p> <p>Population inversion exists and incoming photon induces emission</p>	
<p><b>Multiphoton absorption</b></p> <p>Absorption of two or more photons simultaneously.</p>	
<p><b>Carrier multiplication</b></p> <p>More than one exciton is created: Example of bi-exciton i.e. creation of two excitons on one state.</p>	

<p><b>Transparency</b></p> <p>For a ground state containing two electrons, excitation of one electron can lead to: a photon excitation of the ground-state electron, which is absorbed. The medium is transparent because there is no net gain or loss of photons.</p>	
<p><b>Optical gain</b></p> <p>Optical gain may occur when there are more electrons in the excited state than in the ground state-population inversion. If the gain from stimulated emission is larger than losses due to absorption or scattering of photons, then the system may exhibit amplified stimulated emission.</p>	

### 3.6.4. Three photoexcitation regions

There are three energy regimes to consider: (a)  $E > E_g$ , (b)  $E \sim E_g$ , (c)  $E < E_g$  where  $E$  is the energy of the laser and  $E_g$  is the energy of the semiconductor bandgap. The table below summarizes the various effects and properties, which are then discussed below.

Table 5. Properties and mechanisms for three energy regimes in semiconductor quantum dots.

(a) $E \gg E_g$		(b) $E \sim E_g$		(c) $E < E_g$
Single photon		$E = E_g$	$E < \sim E_g$	Multi-photon
Property: one photon whose energy exceeds $2 E_g$ can create multiple excitons Quantum Yield: $\gg 100\%$		Single photon	Multi-photon	Property(hypothetical): multiple photons whose total energy exceeds $2 E_g$ may create multiple excitons Quantum Yield: $\gg 100\%$ Experiments required
		Property: single photon creates one exciton	Property: multiphotons (simultaneously) create one exciton	
<b>Mechanism: two proposed</b>		<b>Mechanism: Two-level model</b>		<b>Mechanism: unstudied</b>
Nozik et. al. <sup>74</sup>	Klimov et. al. <sup>81-83</sup>			
High energy	High energy			

exciton decays by sequential phonon emission: Coherent	exciton decays by sequential Auger recombinations: Noncoherent process		
---	---	--	--

### 3.6.4.1. Case (a) $E \gg E_g$

In this case a single high energy photon can create multiple excitons resulting in high quantum yields in excess of 100%. The exact mechanism is not clear yet. However, there are two main groups involved in the experimental and theoretical analysis. One is at the National Renewable Energy Laboratory/Univ of Colorado<sup>74</sup> and the other is at Los Alamos National Laboratory<sup>81</sup>. A typical energy level diagram for a semiconductor quantum dot in the ground state with electron population is given in the figure below. Both groups find quantum yields (QY) in excess of 100%--so far up to 700%. This phenomenon does not happen in bulk semiconductors.

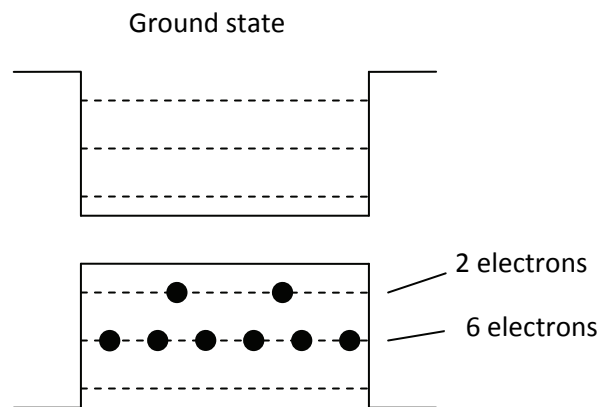


Fig. 19. Schematic diagram of ground state of a semiconductor quantum dot.

The National Renewable Energy Laboratory/Univ of Colorado group measured multiple exciton generation (MEG) for single photon absorption in colloidal PbSe and PbS QDs. Using transient absorption spectroscopy they obtained data for intraband and interband probe energies. The magnitude of the photoinduced absorption change at the band edge is proportional to the number of excitons created. The transients are detected by probing either with a band edge probe pulse or a mid-IR probe pulse. They introduce a model for MEG based on the coherent evolution of the quantum state from the initial single exciton to a coherent superposition of multiple exciton states. The QD cooling via MEG occurring in PbSe is accomplished by energy loss through dephasing of the coherent multiexciton state by phonon emission.

The Los Alamos National Laboratory group also uses transient absorption spectroscopy of CdSe QDs. In this case the multiple exciton formation is denoted as carrier multiplication (CM). The decay mechanism is theorized to be due to nonradiative Auger recombination. These dynamics become increasingly faster as the number of excitons increases. Owing to strong electron-electron interactions, a high-energy electron in the conduction band is not stable, but exists as a virtual electron. This virtual electron loses its energy through the Coulomb interaction



to a valence-band electron. This valence-band electron is then excited to the conduction-band. This process is noncoherent. The figure below shows the two processes.

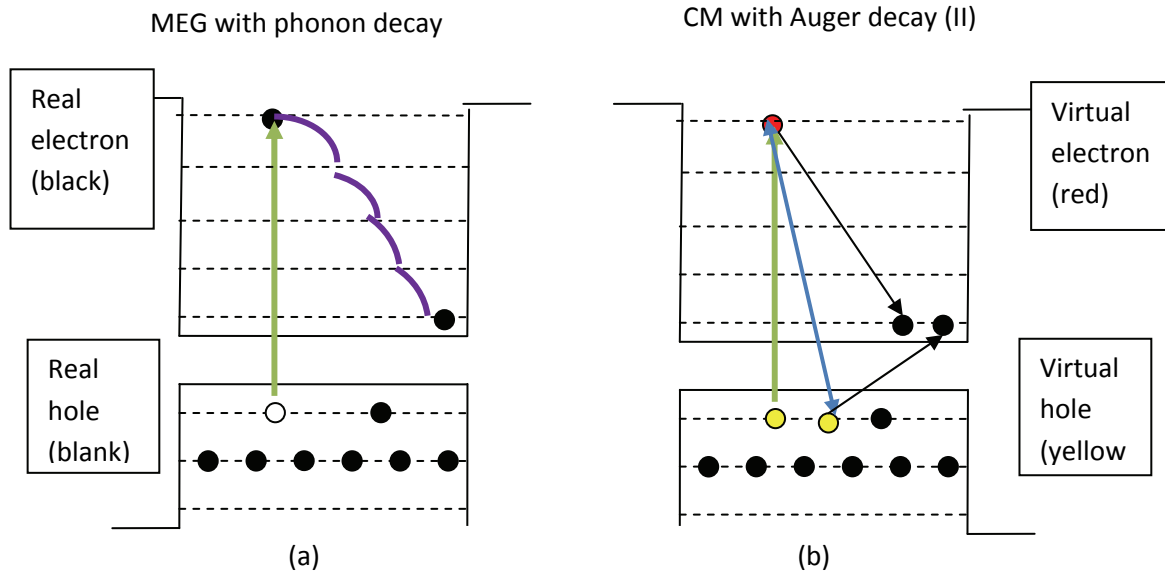


Fig.20. Creation of multiple excitons with single high energy photon. The green arrow represents the high energy absorbed photon. (a) Multiple exciton generation (MEG) with phonon decay<sup>74</sup>. The purple curves represent the phonon decays. (b) Carrier multiplication (CM) with Auger recombination<sup>81</sup>. The blue line represents the Coulomb interaction between the virtual electron and hole. The red dot represents a virtual electron and the yellow dots represent virtual holes.

### 3.6.4.2. Case (b) $E \sim E_g$

This is the most commonly studied as it is the easiest. It appears to follow a two-level model.

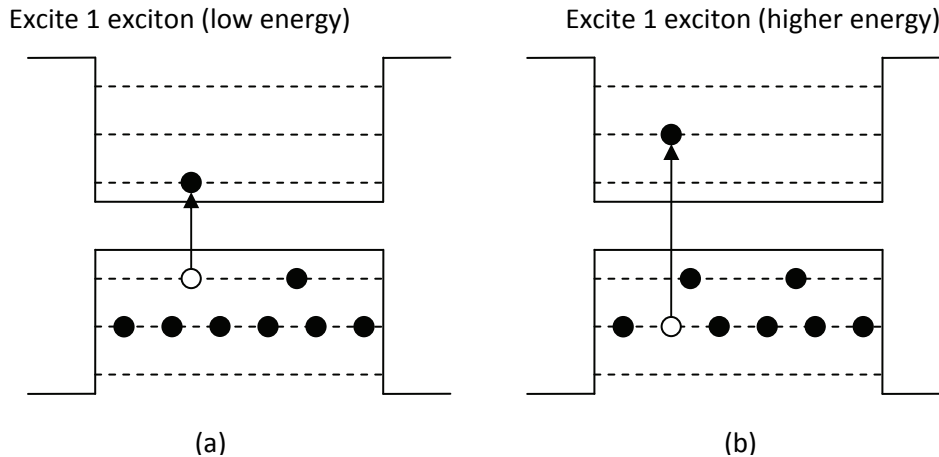


Fig. 21. Creation of a single exciton by an absorbed photon near  $E_g$  (a) Lowest energy ( $1S_{3/2}(h)$  to  $1S(e)$ ). (b) Higher energy ( $1P_{3/2}(h)$  to  $1P(e)$ ).

In the above figure, a single exciton is created by a single photon. Depending on the energy of the incident photon different energy levels can be excited and will appear in the absorption spectrum.

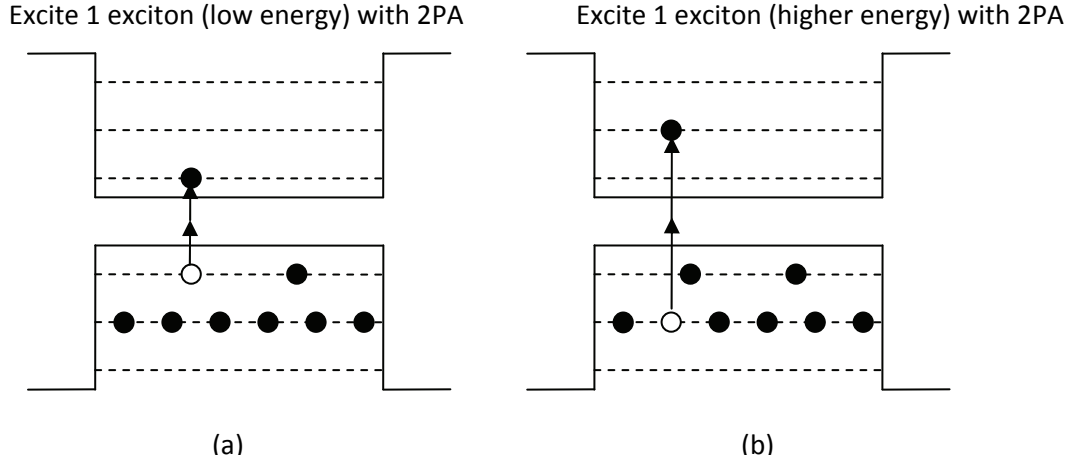


Fig. 22. Creation of a single exciton by multiple (2) photons near  $E_g$  (a) Lowest energy ( $1S_{3/2}(h)$  to  $1S(e)$ ). (b) Higher energy ( $1P_{3/2}(h)$  to  $1P(e)$ ).

In the above figure, a single exciton is created by multiple (e.g. 2) photons. Depending on the energies of the incident photons different energy levels can be excited and the 2PA can be observed in measurements such as z-scan.

The propagation and rate equations are given by 
$$\frac{\partial I}{\partial z} = -[\alpha_0 + \beta I + \sigma_{FCA} N_{e-h}] I, \quad \frac{\partial N_{e-h}}{\partial t} = \frac{\beta I^2}{2\hbar\omega} - \frac{N_{e-h}}{\tau},$$
 where  $\sigma_{FCA}$  is the cross-section for free carrier absorption,  $N_{e-h}$  is the concentration of photoexcited electron-hole pairs,  $\tau$  is the effective decay time,  $\beta$  is the 2PA absorption coefficient.

#### 3.6.4.3. Case (c) $E < E_g$

As far as we know this case has not been studied. It would require a very intense light source and materials with very large nonlinear absorption. Intriguingly, if this case behaves similar to case (a) i.e. single photon absorption, then when multi-photon absorption exceeds  $2E_g$  multiple excitons may be created. As far as we know this has not been experimentally observed, but may be present. This situation is quite interesting because a very high QY may be obtained in this region.

## 4. Conclusions

In this report, we have described results including a time-resolved finite-difference numerical scheme that is more general than traditional techniques. The method was validated against both published research and internal AFRL experiments. Additionally, we expanded our method to include electric field propagation and diffraction effects. Finally, we investigated semiconductor quantum dots in terms of fabrication techniques, electronic energy levels and absorption/recombination phenomena.

## 5. References

1. L. W. Tutt and T. F. Boggess, "A review of optical limiting mechanisms and devices using organics, fullerenes, semiconductors and other materials," *Prog. Quantum. Elect.*, **17**, pp.299-338 (1993).
2. J. A. Hermann and J. Staromlynska, "Special issue on optical limiters, switches and discriminators," *J. Nonlinear Opt. Phys. and Materials*, **2** (1993).
3. K. A. Nguyen, P. N. Day & R. Pachter, *J. Chem. Phys.* **110** 9135 (1999); K. A. Nguyen, P. N. Day & R. Pachter, *J. Phys. Chem.* **103** 7378 (1999); K. A. Nguyen, P. N. Day & R. Pachter, *J. Phys. Chem.* **104** 4755 (2000).
4. R. Crane, K. Lewis, E. W. Van Stryland, and M. Khoshnevisan, *Materials for Optical Limiting*, vol. 374, Materials Research Society, Boston, 1994.
5. R. Sutherland, R. Pachter, P. Hood, D. J. Hagan, K. Lewis, and J. Perry, *Materials for Optical Limiting II*, vol. 479, Materials Research Society, San Francisco, 1997.
6. J. W. Perry, "Organic and metal-containing reverse saturable absorbers for optical limiters," in *Nonlinear Optics of Organic Molecules and Polymers*, H. S. Nalwa and S. Miyata, Ed. Boca Raton, FL: CRC, 1997, pp.813-839.
7. E. W. Van Stryland, D. J. Hagan, T. Xia, and A. A. Said, "Application of nonlinear optics to passive optical limiting," in *Nonlinear Optics of Organic Molecules and Polymers*, H. S. Nalwa and S. Miyata, Ed. Boca Raton, FL: CRC, 1997, pp. 841-860.
8. D. J. Hagan, "Optical limiting," in *Handbook of Optics*, vol. IV, M. Bass, J. M. Enoch, E. W. Van Stryland, and W. L. Wolfe, Eds. New York, NY: McGraw Hill, 2001, pp. 19.1-19.16.
9. L. Brzozowski and E. H. Sargent, "Nonlinear distributed-feedback structures as passive optical limiters," *J. Opt. Soc. Am. B* **17**, pp.1360-1365 (2000).
10. E. W. Van Stryland, M. J. Soileau, S. Ross and D. J. Hagan, "Passive Optical Limiting: Where are we?," *Nonlinear Opt.* **21**, pp.29-38 (1999).
11. P. N. Day, Z. Wang & R. Pachter, *J. Mol. Struct. Theochem* **455** 33 (1998); V. Mastyukov, C-Y. Ruan, M. Fink, Z. Wang, & R. Pachter, *J. Mol. Structure* **556** 225 (2000).
12. B. J. Bacskaï, J. Skoch, G.A. Hickey, R. Allen, and B. T. Hyman, "Fluorescence resonance energy transfer determinations using multiphoton fluorescence lifetime imaging microscopy to characterize amyloid-beta plaques," *J. Biomed Optics* **8**, 368 (2003).
13. E.S. Marmur, C. D. Schmults, and D. J. Goldberg, "A review of laser and photodynamic therapy for the treatment of nonmelanoma skin cancer," *Dermatol. Surg.* **30**, 264 (2004).
14. J. E. Rogers, J. E. Slagle, D. G. McLean, R. L. Sutherland, B. Sankaran, R. Kannan, L.-S. Tan, and P. A. Fleitz, "Understanding the one-photon photophysical properties of a two-photon absorbing chromophore," *J. Phys. Chem. A* **108**, 5514 (2004).
15. J. W. Perry, "Organic and metal-containing reverse saturable absorbers for optical limiters," in *Nonlinear Optics of Organic Molecules and Polymers*, H. S. Nalwa and S. Miyata, Ed. Boca Raton, FL: CRC, pp.813-839 (1997).
16. M. J. Potasek, S. Kim, and D. McLaughlin, "All optical power limiting", *J. Nonlinear Optical Physics and Materials* **9**, 343 (2000).
17. N. Venkatram, D. N. Rao, and M. A. Akundi, "Nonlinear absorption, scattering and optical limiting studies of CdS nanoparticles," *Opt. Express* **13**, 867 (2005).

18. W. Jia, E. P. Douglas, F. Guo, and W. Sun, "Optical limiting of semiconductor nanoparticles for nanosecond laser pulses", *Appl. Phys. Lett.* **85**, 6326 (2004).
19. S. M. Kirkpatrick, R. R. Naik, and M. O. Stone, "Nonlinear saturation and determination of the two-photon absorption cross section of green fluorescent protein," *J. Phys. Chem. B* **105**, 2867 (2001).
20. S. Maruo and S. J. Kawata, "Two-photon-absorbed near-infrared photopolymerization for three-dimensional microfabridation," *J. Microelectromechanical Systems* **7**, 411 (1998).
21. B.H. Cumpston, S. Ananthavel, S. Barlow, D. L. Dyer, J.E. Ehrlich, L. L. Erskine, A. A. Heikal, S. M. Kuebler, I. Y. Lee, D. McCord-Maughon, J. Qin, H. Rockel, M. Rumi, X. L. Wu, S. R. Marder, and J. W. Perry, "Two-photon polymerization initiators for three-dimensional optical data storage and microfabrication," *Nature* **398**, 51 (1999).
22. G. Witzgall, R. Vrijen, E. Yablonovitch, "Single-shot two-photon exposure of commercial photoresist for the production of three-dimensional structures," *Opt. Lett.* **23**, 1745 (1998).
23. W. Denk, J. H. Strickler and W. W. Webb, "Two-photon laser scanning fluorescence microscopy," *Science* **248**, 73 (1990).
24. H. E. Pudavar, M. P. Joshi, P. N. Prasad, and B. A. Reinhardt, "High-density three-dimensional optical data storage in a stacked compact disk format with two-photon writing and single photon readout," *Appl. Phys. Lett.* **74**, 1338 (1999).
25. P. N. Prasad, "Emerging opportunities at the interface of photonics, nanotechnology and biotechnology," *Mol. Cryst. Liq. Cryst.* **415**, 1 (2004).
26. M. Albota, D. Beljonne, J. L. Bredas, J.E. Ehrlich, J. F. Fu, A. A. Heikal, S. E. Hess, T. Kogej, M. D. Levin, S. R. Marder, D. McCord-Maughon, J. W. Perry, H. Rochel, M. Rumi, G. Subramaniam, W. W. Webb, X. L. Wu, and C. Xu, "Design of organic molecules with large two-photon absorption cross sections," *Science* **281**, 1653 (1998).
27. B. A. Reinhardt, L. L. Brott, S. J. Clarson, A. G. Dillard, J. C. Bhatt, R. Kannan, L. Yuan, G. S. He, and P. N. Prasad, "Highly active two-photon dyes: Design, synthesis, and characterization toward application," *Chem. Mater.* **10**, 1863 (1998).
28. J. Kleinschmidt, S. Rentsch, W. Tottleben, and B. Wilhelmi, "Measurement of strong nonlinear absorption in stilbene-choloform solution, explained by the superposition of two-photon absorption and one-photon absorption from the excited state," *Chem. Phys. Lett.* **24**, 133 (1974).
29. D.A. Oulianov, I. V. Tomov, A.S. Dvornikow, and R. M. Rentzepis, "Observations on the measurements of two-photon absorption cross-section," *Opt. Comm.* **191**, 235 (2001).
30. S. Guha, K. Kang, P. Porter, J.F. Roach, D. E. Remy, F. J. Aranda, and D.V.G.L.N. Rao, "Third-order optical nonlinearities of metallotetrabenzoporphyrins and a platinum polyyne," *Opt. Lett.* **17**, 264 (1992).
31. R. L. Sutherland, M. C. Brant, J. Heinrichs, J. E. Rogers, J. E. Slagle, D. G. McLean, and P. A. Fleitz, "Excited state characterization and effective three-photon absorption model of two-photon-induced excited state absorption in organic push-pull charge-transfer chromophores," *J. Opt. Soc. Am. B* **22**, 1939 (2005)..
32. G. S. He, T.-C. Lin, J. Dai, P. N. Prasad, R. Kannan, A. G. Dombroskie, R. A. Vaia, and L.-S. Tan, "Degenerate two-photon-absorption spectral studies of highly two-photon active organic chromophores," *J. Chem. Phys.* **120**, 5275 (2004).
33. P.N. Butcher and D. Cotter, *The Elements of Nonlinear Optics* (Cambridge University Press, Cambridge, UK, 1990).

34. L. Allen and J. H. Eberly, *Optical resonance and two-level atoms* (Plenum Press, New York, 1975).
35. A. I. Maimistov and A. M. Basharov, *Nonlinear Optical Waves* (Kluwer Academic Publishers, Dordrecht, The Netherlands 1999).
36. R. L. Sutherland, *Handbook of nonlinear optics* (Marcel Dekker, New York, 2003).
37. J. Moloney and A. Newell, *Nonlinear Optics* (Westview Press, Boulder, CO, 2004).
38. C. W. Gardiner and M. J. Collet, "Input and output in damped quantum systems: Quantum stochastic differential equations and the master equation", *Phys. Rev. A*, **31**, 3761 (1985).
39. C. W. Gardiner and A.S. Parkins, "Driving ato with light of arbitrary statistics", *Phys. Rev. A*, **50**, 1792 (1994).
40. M. Lax, "Quantum noise IV. Quantum theory of noise sources", *Phys. Rev.* **145**, 110 (1966).
41. A. Barchielli, "Measurement Theory and stochastic differential equations in quantum mechanics", *Phys. Rev. A* **34**, 1642 (1986).
42. M. Klessinger and J. Michl, *Excited States and Photochemistry of Organic Molecules* (VCH, Deerfield Beach, Fl. 1995).
43. D. G. McLean, R. L. Sutherland, M. C. Brant, D. M. Brandelik, P. A. Fleitz, and T. Pottenger, "Nonlinear absorption study of a C60-toluene solution," *Opt. Lett.* **18**, 858 (1993).
44. D.-Y. Wang, C.-L. Zhan, Y. Chen, Y.-J. Li, Z.-Z. Lu, and Y.-Z. Nie, "Large optical power limiting induced by three-photon absorption of two stibazolium-like dyes," *Chem. Phys. Lett.* **369**, 621 (2002).
45. R. Kannan, G. S. He, T.-C. Lin, P. N. Prasad, R. A. Vaia, and L.-S. Tan, "Toward highly active two-photon absorbing liquids. Synthesis and characterization of 1,3,5-triazine-based octupolar molecules," *Chem. Mater.* **16**, 185 (2004).
46. B. E. A. Saleh and M. Teich, *Fundamentals of Photonics*, John Wiley & Sons, Cambridge University Press, 1991. pp. 384-591
47. S.Kirkpatrick et. al., "Nonlinear Saturation and Determination of the Two-Photon Absorption Cross Section of Green Fluorescent Protein", *J. Phys. Chem. B* **2001**, 2867 (2001).
48. S. P. Gubin, N. A. Kataeva and G. B. Khomutov, *Russian Chem Bull, Int. Ed.*, **54**, 827 (2005).
49. T. Sugimoto, *Monodispersed Particles*, Elsevier, New York, 2002.
50. J.H.Fendler and I. Dekany, eds, *Nanoparticles in Solids and Solutions*, Kluwer Academic Publishers, Boston, 1996.
51. Al. Efros and A. L. Efros, *Sov. Phys. Semicond.* **16**, 772 (1982).
52. A. I. Ekimov, Al. L. Efros and A. A. Onushchenko, *Sov. Phys. JETP Lett*, **40**, 1136 (1984).
53. R. Rossetti, S. Nakahara and L.E. Brus, *J. Chem. Phys.* **79**, 1086 (1983).
54. H. Weller, *Ber. Bunsenges. Phys. Chem.* **95**, 1361 (1991).
55. A. Henglein, *Chem. Rev.* **89**, 1861 (1989).
56. A. Eychmuller, *J. Phys. Chem B*, **42**, 6514 (2000)
57. U. K. Gautam, M. Ghosh, and C. N. R. Rao, *Chem. Phys. Lett.* **12**, 75 (1999).
58. P. Lianos and J. K. Thomas, *Chem. Phys. Lett.* **125**, 299 (1986).
59. F. Seker, K. Meeker, T. F. Fuch, and A. B. Ellis, *Chem. Rev.* **100**, 2505 (2000).

60. S. Park, B. L. Clark, D. A. Keszler, J. P. Bender, J. F. Wager, T. A. Renolds and G. S. Herman, *Science*, **297**, 65 (2002).
61. M. Grundman, N. N. Ledentsov, N. Kirstaedter, F. Heinrichsdorff, A. Krost, D. Bimberg, A. O. Kosogov, S. S. Ruvimov, P. Werner, V. M. Ustinov, P.S. Kopev, and Zh. I. Alferov, *Thin Solid Films* **318**,83 (1998).
62. T. Nakanishi, B. Ohtani, and K. Uosaki, *J. Phys. Chem. B* **102**, 1571 (1998).
63. K. Prabhakaran, F. Meneau, G. Sankar, K. Sumitomo, T. Murashita, Y. Homma, G. N. Greaves and T. Ogino, *Adv. Mater*, **15**, 1522 (2003).
64. C. A. Constantine, K. M. Gattas-Asfura, S. V. Mello, G. Grespo, V. Rastogi, T. C. Cheng, J. J. DeFrank and R. M. Leblanc, *Langmuir* **19**, 9863 (2003).
65. R. D. Stramel, T. Nakamura, and J. K. Thomas, *J. Chem. Soc. Faraday Trans. 1*, **84**, 1287 (1998).
66. B. Marder, U. Oberhagemann, S. Vortmann and H. Gies, *Mesoporous Mater.* **6**, 375 (1996).
67. T. Hirai, M. Nanba, and I. Komasaawa, *J. Colloid and Interface Sci.* **268**, 394 (2003).
68. S. C. Farne and T.E. Patten, *Chem. Mater.* **13**, 3920 (2001).
69. W. Caseri, *Macromol. Rapid Commun.* **21**, 705 (2000).
70. L. Brus, *Appl. Phys.A* **53**, 465 (1991).
71. Al. Efros and A. Efros, *Sov. Phys. Sem.* **16**, 772 (1982).
72. A. Alivisatos, *Science* **271**, 933 (1996).
73. Al. Efros and M. Rosen, *Annu. Rev. Mater. Sci.* **30**, 475 (2000).
74. R. J. Ellington, M.C. Beard, J. C. Johnson, P. Yu, O.I. Miclc, A. J. Nozik, A. Shabaev and A. L. Erfos, *Nano Lett.* **5**, 865 (2005).
75. C. Kittel, *Introduction to Solid State Physics* (John Wiley, NY, 2005).
76. V. Klimov, *Los Alamos Science*, issue 23, p. 214 (2003).
77. V. Klimov, *Science* **287**, 1011 (2000).
78. A. P. Alivisatos, *J. Phys. Chem.* **100**, 13226-13239 (1996).
79. A. Zunger, *MRS Bulletin*, 35 (1998).
80. L. Wang and A. Zunger, *J. Phys. Chem. B* **102**, 6549 (1998).
81. V. I. Klimov, *Annu. Rev. Phys. Chem.* **58**, 635 (2007).
82. R. D. Shaller and V. I. Klimov, *Phys. Rev. Lett.* **92**, 186601 (2004).
83. R. D. Schaller, V. M. Agranovich, and V. I. Klimov, *Nature Phys.* **1**, 189 (2005).
84. S. Kim and M. Potasek, "Numerical study of short optical pulse propagation in nonlinear reverse saturable absorbers", AFRL Technical report, 2001.
85. E. Parilov and M. Potasek, "Method, System and Software Arrangement for Determining an Interaction Between an Electromagnetic Radiation and a Material", US2007/0290147 A1, Dec. 2007.

## Appendix A Description of the Numerical Method

We introduce a family of identical 2D grids  $\Omega$  indexed by radius  $\rho$ , such that

$$\Omega = \{\Omega(\rho_j), \rho_j = j\Delta\rho\}, \quad (\text{A1})$$

$$\Omega(\rho_j) = (\Omega_{\tilde{n}}(j), \Omega_{\tilde{i}}(j)), \quad (\text{A2})$$

For every  $\rho_j$  sample, a member from  $\Omega$  is a pair of interleaved grids in the  $\eta$ - $\tau$  parametric domain, such that one grid is given by

$$\begin{aligned} \Omega_{\tilde{n}}(j) &= \{(\eta_{n+1/2}, \rho_j, \tau_{i+1/2}), \\ \eta_{n+1/2} &= (\eta_0 + \Delta\eta/2) + n\Delta\eta, \tau_{i+1/2} = (\tau_0 + \Delta\tau/2) + i\Delta\tau\}, \end{aligned} \quad (\text{A3})$$

and is used to sample the population density  $\mathbf{N}(\eta, \rho, \tau)$ . Another grid given by

$$\Omega_{\tilde{i}}(j) = \{(\eta_n, \rho_j, \tau_i), \eta_n = \eta_0 + n\Delta\eta, \tau_i = \tau_0 + i\Delta\tau\} \quad (\text{A4})$$

is used to sample the intensity  $\tilde{I}(\eta, \rho, \tau)$ . We integrate the resulting dimensionless equations given by Eqs. (9) and (10) for a small step sizes  $\Delta\tau, \Delta\eta$  at  $\Omega_{\tilde{n}}(j), \Omega_{\tilde{i}}(j)$  grid points correspondingly in two steps. In the first step we integrate the system of the rate equations to find a spatially-resolved solution in the current moving frame (reference system of the “pulse rest”), while keeping the average intensity  $\frac{1}{2}[I(\eta_n, \rho_j, \tau_i) + I(\eta_{n+1}, \rho_j, \tau_i)]$  fixed. In the second step we solve the propagation equation for a thin slice  $[\eta, \eta + \Delta\eta]$ , by using available average population density  $\frac{1}{2}[\mathbf{N}(\eta_{n+1/2}, \rho_j, \tau_{i-1/2}) + \mathbf{N}(\eta_{n+1/2}, \rho_j, \tau_{i+1/2})]$  as an approximation for electronic populations (see Appendix B for detailed derivation). The resulting system of coupled equations, given by Eqs. (A5) and (A6), still has interdependences between the intensity and population densities; therefore, we do  $k=1:K$  iterations to obtain a numerical solution of the intensity function  $I(\eta_n, \rho, \tau)$  for a given depth  $\eta_n$  (for notational simplicity only the indices  $n, j$ , and  $i$  will be kept in the following sections of the paper). The coupled equations are given by

$$\begin{aligned} \mathbf{N}_{n+1/2,j,i+1/2}^{(k)} &\approx \exp\left(\Delta\tau T_0 \hat{D}_0 + \Delta\tau T_0 \frac{\hat{D}_1 I_0}{\hbar\omega_0} \frac{1}{2}\{I_{n,j,i} + I_{n+1,j,i}^{(k)}\} \right. \\ &\quad \left. + \Delta\tau T_0 \frac{\hat{D}_2 I_0^2}{2\hbar\omega_0} \frac{1}{2}\{I_{n,j,i}^2 + I_{n+1,j,i}^{(k)2}\} + \Delta\tau T_0 \frac{\hat{D}_3 I_0^3}{3\hbar\omega_0} \frac{1}{2}\{I_{n,j,i}^3 + I_{n+1,j,i}^{(k)3}\}\right) \mathbf{N}_{n+1/2,j,i-1/2}^{(k)} \\ I_{n+1,j,i}^{(k+1)} &\approx \exp\left(-L_{df} N \Delta\eta \left\{\boldsymbol{\sigma}_1 \cdot \frac{\mathbf{N}_{n+1/2,j,i-1/2}^{(k)} + \mathbf{N}_{n+1/2,j,i+1/2}^{(k)}}{2}\right\} \right. \\ &\quad \left. - L_{df} N \Delta\eta I_0 \left\{\boldsymbol{\sigma}_2 \cdot \frac{\mathbf{N}_{n+1/2,j,i-1/2}^{(k)} + \mathbf{N}_{n+1/2,j,i+1/2}^{(k)}}{2}\right\} \frac{1}{2}\{I_{n,j,i} + I_{n+1,j,i}^{(k)}\}\right) \end{aligned} \quad (\text{A5})$$

$$-L_{df} N \Delta \eta I_0^2 \left\{ \sigma_3 \cdot \frac{\mathbf{N}_{n+1/2,j,i-1/2}^{(k)} + \mathbf{N}_{n+1/2,j,i+1/2}^{(k)}}{2} \right\} \frac{1}{2} \{ I_{n,j,i}^2 + I_{n+1,j,i}^{(k)2} \} I_{n,i} \quad (\text{A6})$$

We found that at any depth  $\eta_n$  the resulting iterating scheme given by Eqs. (A5) and (A6) converges very fast with a second-order Taylor series expansion of the matrix exponential in Eq. (A5). By selecting a sufficiently small  $\Delta\tau$ , we can keep the number of iterations  $k$  to 2 or 3. However, for pulses that are short in the temporal domain, the grid size must be significantly increased to ensure that eigenvalues of the matrix in the exponent are less than one, making the Taylor expansion possible. An alternative way is to sub-sample the grid on demand, i.e. only at the high intensity areas, which are relatively small compared to entire parametric domain. At every time step  $\tau_{i-1/2} \rightarrow \tau_{i+1/2}$  in Eq. (A5), we check the magnitude of the elements of the matrix in the exponent. If necessary, we introduce additional  $M-1$  time sub-samples, such as  $\tau_{i-1/2} = \tau^0 \rightarrow \tau^1 \rightarrow \dots \tau^{M-1} \rightarrow \tau_{i+1/2} = \tau^M$ , where  $M$  is chosen such that the elements of the resulting refined matrices corresponding to those sub-samples are small enough to ensure the validity of the Taylor series approximation of their matrix exponentials [which are described later in Eq. (A9)]. To calculate the refined matrices for every such  $\tau^m$ , we repeat the same integration step, which was done to derive Eq. (A5) with the only difference being that now the integration domain is given by  $[\tau^m, \tau^{m+1}]$ . During such integration, we also need to estimate the average intensity values at  $\hat{\tau}^m = \tau^m + 1/2 \Delta\tau'$  samples, where  $\Delta\tau' = \tau^{m+1} - \tau^m \equiv \Delta\tau / M$  is the resulting sub-sampling time step. As any such sample  $\hat{\tau}^m$  is equal to  $\tau_{i-1/2} + (m+1/2)\Delta\tau'$ , we estimate  $I_{n,j}(\hat{\tau}^m) \equiv I(\eta_n, \rho_j, \hat{\tau}^m)$  by a linear interpolation of  $I_{n,j}(\tau_{i-1/2})$  and  $I_{n,j}(\tau_{i+1/2})$  given by

$$I_{n,j}(\hat{\tau}^m) = I_{n,j}(\tau_{i-1/2} + (m+1/2)\Delta\tau') \\ = \lambda_m I_{n,j}(\tau_{i-1/2}) + \mu_m I_{n,j}(\tau_{i+1/2}), \quad (\text{A7})$$

where  $\lambda_m + \mu_m = 1$ ,  $\lambda_m = (1 - (m+1/2)/M)$ . The powers of the intensity values  $I_{n,j}^\alpha$ ,  $\alpha = 1..3$ , for the half-way time grid samples  $\tau_{i-1/2}$ ,  $\tau_{i+1/2}$  in Eq. (A7) are interpolated by

$$I_{n,j}^\alpha(\tau_{i-1/2}) \approx (I^\alpha)_{n,j,\hat{i}} \equiv \frac{1}{2} (I_{n,j,\hat{i}-1}^\alpha + I_{n,j,\hat{i}}^\alpha). \quad (\text{A8})$$

Finally, taking into account Eqs. (A7) and (A8), for every affected time sample the refined version of Eq. (A5) is given by

$$\mathbf{N}_{n+1/2,j,i+1/2}^{(k)} \approx \prod_{m=0}^{M-1} \exp \left\{ \frac{\Delta\tau T_0}{M} \left[ \hat{D}_0 + \sum_{\alpha=1}^{N_A} \frac{\hat{D}_\alpha I_0^\alpha}{\alpha \hbar \omega_0} \right. \right. \\ \left. \left. \times \left( \lambda_m \frac{1}{2} \left\{ (I^\alpha)_{n,j,\hat{i}} + (I^\alpha)_{n+1,j,\hat{i}}^{(k)} \right\} + \mu_m \frac{1}{2} \left\{ (I^\alpha)_{n,j,\hat{i}+1} + (I^\alpha)_{n+1,j,\hat{i}+1}^{(k)} \right\} \right) \right] \right\} \mathbf{N}_{n+1/2,j,i-1/2}^{(k)}, \quad (\text{A9})$$

where  $M$  is chosen to make the elements of the matrix in the exponent of Eq. (A5) smaller than a given threshold i.e.  $0 < \varepsilon < 1$ , such that



$$M \equiv M(n, j, i) = \min_{u,v} \left\{ M', \frac{\Delta \tau T_0}{M'} \times \left| \begin{aligned} & \hat{d}_{u,v}^0 \\ & + \frac{I_0}{\hbar \omega_0} \frac{1}{2} \{ I_{n,j,i} + I_{n+1,j,i}^{(k)} \} \hat{d}_{u,v}^1 \\ & + \frac{I_0^2}{2\hbar \omega_0} \frac{1}{2} \{ (I^2)_{n,j,i} + (I^2)_{n+1,j,i}^{(k)} \} \hat{d}_{u,v}^2 \\ & + \frac{I_0^3}{3\hbar \omega_0} \frac{1}{2} \{ (I^3)_{n,j,i} + (I^3)_{n+1,j,i}^{(k)} \} \hat{d}_{u,v}^3 \end{aligned} \right| < \varepsilon \right\}. \quad (\text{A10})$$

The analysis of nonlinear materials is often guided by measurements of the optical transmission. In most calculations the radial domain is assumed to be constant but by using both the radial and temporal profiles of the solution, we can now analyze and compare the transmission plots of the peak transmittance  $T_\delta$ , defined by Eq. (A11), and the integrated transmittance  $T_E$ , given by Eq. (A12) (with  $T_F$  as a cumulative Fresnel transmittance at the interfaces)

$$T_\delta = \max_{\rho, \tau} \frac{\delta E_{out}(\rho, \tau)}{\delta E_{in}(\rho, \tau)} \approx \max_{\rho, \tau} \frac{T_F I(\eta_{\max}, \rho, \tau)}{I_0 \exp\{-\tau^2\} \exp\{-\rho^2\}}, \quad (\text{A11})$$

$$T_E = \frac{E_{out}}{E_{in}} = \frac{\int_0^{+\infty} d\rho' 2\pi\rho' \int_{-\infty}^{+\infty} d\tau' I(\eta_{\max}, \rho', \tau')}{2\pi \int_0^{+\infty} d\rho' \rho' \int_{-\infty}^{+\infty} d\tau' I_0 e^{-(\tau')^2} e^{-(\rho')^2}}. \quad (\text{A12})$$

The integrated value  $T_E$  is generally accepted as a key parameter quantifying nonlinear materials because it can be measured in the laboratory using widely available thermal detectors, which average the pulse intensity over space and time. However, as the peak intensity often causes damage to opto-electronic detectors and sensors, it is useful to have a numerical check on the validity of the laboratory measurements using thermal detectors. Because pulse distortion can occur in both the temporal and radial domains, our calculation can also search the radial and temporal domains of the pulse to find the maximum value of the intensity to use in the calculation of  $T_\delta$ .

## Appendix B. Description of Contribution to Each Energy Level

We define the total intensity reduction  $Q_\omega$  for a given grid index  $\omega = \{n+1/2, j, i-1/2\}$  as the product of individual reductions  $Q_{s;\omega}$  due to electronic levels  $s$  with nontrivial absorption cross-sections:

$$Q_\omega = \prod_{s \in S_\sigma} Q_{s;\omega},$$

$$S_\sigma = \{s \mid \sigma_1[s] + \sigma_2[s] + \sigma_3[s] > 0\}. \quad (\text{B1})$$

The individual reductions  $Q_{s;\omega}$  come from Eq. (A6). They equal to the corresponding exponential terms responsible for intensity decrease at the final iteration,  $k = K$ , and are given by:

$$Q_{s;\omega} \equiv Q_{s;n+1/2,j,i-1/2} = \exp \left( -L_{df} N \Delta \eta \sum_{\beta=1}^{N_B} I_0^{\beta-1} \right. \\ \left. \times \left\{ \sigma_\beta[s] \cdot \frac{N_{s;n+1/2,j,i-1/2}^{(K)} + N_{s;n+1/2,j,i+1/2}^{(K)}}{2} \right\} \frac{1}{2} \left\{ I_{n,j,i}^{\beta-1} + I_{n+1,j,i}^{(K)\beta-1} \right\} \right). \quad (\text{B2})$$

As we are interested in relative contributions, we introduce the intensity decay values as follows:

$$q_\omega = 1 - Q_\omega, \quad (\text{B3})$$

$$p_{s;\omega} = 1 - Q_{s;\omega}. \quad (\text{B4})$$

The total intensity decay values  $q_\omega$  are used to analyze what part of the pulse mostly decreases at a given depth value. Meanwhile, the intensity decay  $p_{s;\omega}$  due to level  $s$ , in turn, defines the relative contribution  $\hat{p}_{s,\omega}$  by the following formula

$$\hat{p}_{s;\omega} = p_{s;\omega} / \sum_{s' \in S_\sigma} p_{s';\omega}. \quad (\text{B5})$$

Nonlinear dependency of the relative contributions  $\hat{p}_{s,\omega}$  on the population densities and intensities confirms that it may be not accurate to approximate such contributions from the available values of the population densities. In sections above we first plot total intensity decays  $q_{\{\omega\}}$ , and secondly, we superimpose plots of absolute contributions  $q_{s;\{\omega\}}$  derived from relative contributions  $\hat{p}_{s,\{\omega\}}$  by scaling them to the total intensity decays:

$$q_{s;\{\omega\}} = \hat{p}_{s,\{\omega\}} \cdot q_{\{\omega\}}. \quad (\text{B6})$$

By using this feature in analyzing certain nonlinear materials, we explained why our numerical scheme is as good as the other techniques in some cases, while gives better solution in other cases, and we outlined our hypothesis on why all techniques fail in the case of high input energies.

## Appendix C Numerical Method in terms of Electric Field<sup>84,85</sup>

A numerical scheme to solve the rate equation (23) is described here. An iteration formula that may be used to solve this equation numerically can be written as:

$$\mathbf{N}_{n+1/2,j,i+1/2} \approx \exp\left(\delta D_0 + \sum_{\alpha=1}^{N_A} \delta D_{\alpha} \frac{1}{2} \{\bar{Q}_{n,j,i}^{\alpha} + \bar{Q}_{n+1,j,i}^{\alpha}\}\right) \mathbf{N}_{n+1/2,j,i-1/2} \quad , \quad (C1)$$

where  $\delta D_{\alpha} \equiv \Delta \tau D_{\alpha}$ ,  $\alpha \in [0 \dots N_A]$ . This equation can be expressed in operator form as:

$$\bar{\mathbf{N}}_{i+1/2}^{n+1/2} \approx e^{\Delta \tau \Upsilon^{\bar{Q}}[n]} \bar{\mathbf{N}}_{i-1/2}^{n+1/2} \quad , \quad \text{or} \quad \bar{\mathbf{N}}_{i+1/2}^{n+1/2} \approx \exp\left(\Delta \tau \left\{ \Upsilon_0 + \sum_{\alpha=1}^{N_A} \Upsilon_{\alpha}^{\bar{Q}}[n] \right\}\right) \bar{\mathbf{N}}_{i-1/2}^{n+1/2} \quad , \quad (84)(C2)$$

with  $\bar{\mathbf{N}}_{i+1/2}^{n+1/2} \equiv [\mathbf{N}_{n+1/2,0,i-1/2}, \dots, \mathbf{N}_{n+1/2,j,i-1/2}, \dots, \mathbf{N}_{n+1/2,N_r,i-1/2}]$  and  $\mathbf{N}_{n+1/2,j,i-1/2} \equiv \mathbf{N}(\eta_{n+1/2}, \rho_j, \tau_{i-1/2})$ .

The parameter  $\Upsilon_{\alpha}^{\bar{Q}}[n] \equiv D_{\alpha} \frac{1}{2} \{\bar{Q}_{n,j,i}^{\alpha} + \bar{Q}_{n+1,j,i}^{\alpha}\}$  may be considered as a discretization of  $\Upsilon_{\alpha}^{\bar{Q}}(\eta, \tau)$  and can be used in the expression for the rate operator with  $\bar{Q}_{n,j,i} \equiv \bar{Q}(\eta_n, \rho_j, \tau_i)$ . A general solution for the propagation equation (33) can be expressed as:

$$\begin{aligned} Q(\eta + \Delta \eta) &= \exp\left\{ \int_{\eta}^{\eta + \Delta \eta} (\Phi(\eta', \tau) + \Psi(\rho, \tau)) d\eta' \right\} \circ Q(\eta) \\ &= \exp\left\{ \int_{\eta}^{\eta + \Delta \eta} \Phi(\eta', \tau) d\eta' + \Psi(\rho, \tau) \Delta \eta \right\} \circ Q(\eta) \quad . \end{aligned} \quad (C3)$$

A symmetric split-step (Fourier) technique can be used to solve this propagation equation. A value at a subsequent depth sample is determined from the value at a current depth sample by first applying a diffraction operator along  $\Delta \eta$  while neglecting a rate operator, and then applying the rate operator to the resulting  $Q$  value while neglecting the diffraction operator. Mathematically, this is equivalent to a commuting of the rate and the diffraction operators, which is expressed as:

$$Q(\eta + \Delta \eta) \approx \exp\left( \int_{\eta}^{\eta + \Delta \eta} \Phi(\eta', \tau) d\eta' \right) e^{\Delta \eta \Psi(\rho, \tau)} \circ Q(\eta) \quad . \quad (C4)$$

Such operators may not generally commute, and an error introduced by this approximation can be on the order of  $\Delta \eta$ . To decrease the computational error, a symmetric version of the split-step procedure can be used, which may be described by the following equation:

$$Q(\eta + \Delta \eta) \approx e^{\frac{\Delta \eta}{2} \Psi(\rho, \tau)} \exp\left( \int_{\eta}^{\eta + \Delta \eta} \Phi(\eta', \tau) d\eta' \right) e^{\frac{\Delta \eta}{2} \Psi(\rho, \tau)} \circ Q(\eta) \quad . \quad (C5)$$

An expression for the rate-related operator is derived by using the following approximation:

$$\begin{aligned}
\exp\left(\int_{\eta}^{\eta+\Delta\eta} \Phi(\eta', \tau) d\eta'\right) &= \exp\left(\int_{\eta}^{\eta+\Delta\eta} d\eta' \left\{ -\sum_{\beta=1}^{N_B} \Phi_{\beta}^N(\eta', \tau) \Phi_{\beta}^Q(\eta', \tau) - \Phi_L \right\}\right) \\
&= \exp(-\Phi_L \Delta\eta) \prod_{\beta=1}^{N_B} \exp\left(\int_{\eta}^{\eta+\Delta\eta} \Phi_{\beta}^N(\eta', \tau) \Phi_{\beta}^Q(\eta', \tau) d\eta'\right) \\
&\approx \exp(-\Phi_L \Delta\eta) \prod_{\beta=1}^{N_B} \exp\left(\Delta\eta \left\{ \frac{\Phi_{\beta}^N(\eta + \Delta\eta/2, \tau - \Delta\tau/2) + \Phi_{\beta}^N(\eta + \Delta\eta/2, \tau - \Delta\tau/2)}{2} \right\} \right. \\
&\quad \left. \times \left\{ \frac{\Phi_{\beta}^Q(\eta + \Delta\eta, \tau) + \Phi_{\beta}^Q(\eta, \tau)}{2} \right\} \right). \tag{C6}
\end{aligned}$$

Substituting the approximation for the rate operator provided in Eq. (C6) into Eq. (C5) provides a form of the propagation equation which may be expressed as:

$$\begin{aligned}
Q(\eta + \Delta\eta) &\approx e^{\frac{\Delta\eta}{2} \Psi(\rho, \tau)} \exp(-\Delta\eta \Phi_L) \\
&\quad \times \prod_{\beta=1}^{N_B} \exp\left(\Delta\eta \left\{ \frac{\Phi_{\beta}^N(\eta + \Delta\eta/2, \tau - \Delta\tau/2) + \Phi_{\beta}^N(\eta + \Delta\eta/2, \tau - \Delta\tau/2)}{2} \right\} \right. \\
&\quad \left. \times \left\{ \frac{\Phi_{\beta}^Q(\eta + \Delta\eta, \tau) + \Phi_{\beta}^Q(\eta, \tau)}{2} \right\} \right) e^{\frac{\Delta\eta}{2} \Psi(\rho, \tau)} \circ Q(\eta). \tag{C7}
\end{aligned}$$

A solution for the diffraction equation is obtained by using a Crank-Nicholson scheme. We use the following approximation to the diffraction operator:

$$\Psi_{df}(\rho, \tau) \approx \Psi(\rho) = \frac{i}{4} \nabla_{\rho}^2. \tag{C8}$$

Applying a differential operator  $\exp(\Psi(\rho) \Delta\eta/2) \circ Q(\eta)$  is equivalent to solving the following differential equation:

$$\frac{\partial Q(\eta, \rho)}{\partial \eta} = \frac{1}{2} \Psi(\rho) \circ Q(\eta, \rho). \tag{C9}$$

Substituting the expression for the diffraction operator provided in Eq. (C8) yields the following equation to be solved:

$$\frac{\partial Q(\eta, \rho)}{\partial \eta} = a_m \nabla_{\rho}^2 Q(\eta, \rho), \tag{C10}$$

where  $a_m \equiv 1/2 \times i/4$  and a time variable is omitted when applying the diffraction operator. A forward difference approximation for the  $\eta$  derivative is written as

$$\frac{\partial Q}{\partial \eta} = \frac{Q_j^{n+1} - Q_j^n}{\Delta\eta}. \tag{C11}$$

A variant of Crank-Nicholson scheme can be used to approximate the Laplacian operator:

$$\nabla_\rho^2 Q(\eta, \rho) \approx \frac{1}{2} \{ \nabla_\rho^2 Q(\eta + \Delta\eta, \rho) + \nabla_\rho^2 Q(\eta, \rho) \}; \quad (C12)$$

$$\begin{aligned} \nabla_\rho^2 Q(\eta_n, \rho) &= \left( \frac{1}{\rho} \frac{\partial}{\partial \rho} + \frac{\partial^2}{\partial \rho^2} \right) Q(\eta_n, \rho) \\ &\approx \left[ \frac{1}{\rho_j} \frac{Q_{j+1}^n - Q_{j-1}^n}{2\Delta\rho} + \frac{Q_{j+1}^n - 2Q_j^n + Q_{j-1}^n}{\Delta\rho^2} \right]. \end{aligned} \quad (C13)$$

Applying these operators results in the following iteration scheme:

$$\begin{aligned} \frac{Q_j^{n+1} - Q_j^n}{\Delta\eta} &\approx \frac{a_m}{4\rho_j\Delta\rho} [Q_{j+1}^{n+1} - Q_{j-1}^{n+1} + Q_{j+1}^n - Q_{j-1}^n] \\ &\quad + \frac{a_m}{2\Delta\rho^2} [Q_{j+1}^{n+1} - 2Q_j^{n+1} + Q_{j-1}^{n+1} + Q_{j+1}^n - 2Q_j^n + Q_{j-1}^n]. \end{aligned} \quad (C14)$$

After grouping the terms containing identical (or substantially similar)  $Q$  samples, the diffraction equation can be expressed in a discrete form as:

$$u_{j-1}^j Q_{j-1}^{n+1} + u_j^j Q_j^{n+1} + u_{j+1}^j Q_{j+1}^{n+1} = v_{j-1}^j Q_{j-1}^n + v_j^j Q_j^n + v_{j+1}^j Q_{j+1}^n, \quad (C15)$$

with:

$$\begin{aligned} u_{j-1}^j &= \frac{a_m \Delta\eta}{2\Delta\rho} \left( \frac{1}{2\rho_j} - \frac{1}{\Delta\rho} \right); \quad u_j^j = 1 + \frac{a_m \Delta\eta}{\Delta\rho^2}; \quad u_{j+1}^j = -\frac{a_m \Delta\eta}{2\Delta\rho} \left( \frac{1}{2\rho_j} + \frac{1}{\Delta\rho} \right); \\ v_{j-1}^j &= -\frac{a_m \Delta\eta}{2\Delta\rho} \left( \frac{1}{2\rho_j} - \frac{1}{\Delta\rho} \right); \quad v_j^j = 1 - \frac{a_m \Delta\eta}{\Delta\rho^2}; \quad \text{and} \quad v_{j+1}^j = \frac{a_m \Delta\eta}{2\Delta\rho} \left( \frac{1}{2\rho_j} + \frac{1}{\Delta\rho} \right). \end{aligned} \quad (C16)$$

Equations (C15) and (C16) are applicable only for “internal” indices  $0 < \rho_j < \rho_{N_r}$ ,  $0 < \rho_1 \leq \rho_j \leq \rho_{N_r-1} < \rho_{N_r}$ , and boundary cases should be evaluated separately.

A solution to the differential equation that includes diffraction effects is obtained at a boundary where  $\rho = 0$ . A derivative  $\partial Q / \partial \rho$  can be zero at  $\rho = 0$  in a system having cylindrical symmetry such as a circular pulse footprint. A limit of the expression  $Q'(\rho) / \rho$  is obtained when  $\rho \rightarrow 0$  by using a Maclaurin expansion:

$$Q'(\rho) = Q'(0) + Q''(0)\rho + o(\rho^2); \quad (C17)$$

$$\frac{Q'(\rho)}{\rho} = Q''(0) + o(\rho^1) \rightarrow Q''(0), \quad (C18)$$

Using Eqs. (C17) and (C18), the diffraction equation at  $\rho = 0$  is written as

$$\frac{\partial Q}{\partial \eta} = 2a_m \frac{\partial^2 Q}{\partial \rho^2}. \quad (C19)$$

A variant of Crank-Nicholson technique is applied to estimate the second derivative term for  $\rho \rightarrow 0$ :

$$\frac{\partial^2 Q}{\partial \rho^2}(\eta_n, 0, \tau) \approx \frac{1}{2} \left\{ \frac{\partial^2 Q}{\partial \rho^2}(\eta + \Delta\eta, 0, \tau) + \frac{\partial^2 Q}{\partial \rho^2} Q(\eta, 0, \tau) \right\}. \quad (C20)$$

A second-order approximation to the second derivative is written as:

$$\frac{\partial^2 Q}{\partial \rho^2}(\eta_{n+1}, 0, \tau) \approx \frac{1}{\Delta \rho^2} \{ Q_{j+1}^{n+1} - 2Q_j^{n+1} + Q_{j-1}^{n+1} \}. \quad (C21)$$

Using Eqs. (C20) and (C21), the diffraction equation at the center of a pulse is written in an approximate form as:

$$\frac{Q_j^{n+1} - Q_j^n}{\Delta \eta} \approx \frac{2a_m}{2\Delta \rho^2} [Q_{j+1}^{n+1} - 2Q_j^{n+1} + Q_{j-1}^{n+1} + Q_{j+1}^n - 2Q_j^n + Q_{j-1}^n]. \quad (C22)$$

The derivative of  $Q$  can be zero with respect to radial distance at  $\rho = 0$ , because the center of the pulse is an extreme value. Parameter values can be approximated at  $j=-1$  as  $Q_{-1}^{n+1} = Q_1^{n+1}$  and  $Q_{-1}^n = Q_1^n$ . Therefore the diffraction equation can be rewritten as follows:

$$\frac{Q_0^{n+1} - Q_0^n}{\Delta \eta} \approx \frac{a_m}{\Delta \rho^2} [2Q_1^{n+1} - 2Q_0^{n+1} + 2Q_1^n - 2Q_0^n]. \quad (C23)$$

Eq. (C23) can be used to obtain the following general equation which is applicable at a center of a pulse (at  $\rho = 0$ ):

$$u_0^0 Q_0^{n+1} + u_1^0 Q_1^{n+1} = v_0^0 Q_0^n + v_1^0 Q_1^n, \quad (C24)$$

where

$$u_0^0 = 1 + \frac{2a_m \Delta \eta}{\Delta \rho^2}; \quad u_1^0 = -\frac{2a_m \Delta \eta}{\Delta \rho^2}; \quad v_0^0 = 1 - \frac{2a_m \Delta \eta}{\Delta \rho^2}; \quad \text{and} \quad v_1^0 = \frac{2a_m \Delta \eta}{\Delta \rho^2}. \quad (C25)$$

A solution to the diffraction equation at an outer boundary of a pulse at  $\rho = \rho_{N_r}$ , can be obtained using a technique similar to that used to find a solution at the center of the pulse described here. A value at a non-existing sample point  $\rho = \rho_{N_r+1}$  can be reconstructed by evaluating a linearly interpolation at values of  $\rho$  near the boundary:

$$\frac{Q_{N_r+1}^n - Q_{N_r}^n}{\Delta \rho} = \frac{Q_{N_r}^n - Q_{N_r-1}^n}{\Delta \rho}. \quad (C26)$$

This linear interpolation leads to a relationship, such as:

$$Q_{N_r+1}^n = 2Q_{N_r}^n - Q_{N_r-1}^n. \quad (C27)$$

Eq. (C27) can be substituted into the general diffraction equation, Eq. (C15) to provide a diffraction equation having a form

$$(\tilde{u}_{N_r-1}^{N_r} - \tilde{u}_{N_r+1}^{N_r}) Q_{N_r-1}^{n+1} + (\tilde{u}_{N_r}^{N_r} + 2\tilde{u}_{N_r+1}^{N_r}) Q_{N_r}^{n+1} = (\tilde{v}_{N_r-1}^{N_r} - \tilde{v}_{N_r+1}^{N_r}) Q_{N_r-1}^n + (\tilde{v}_{N_r}^{N_r} + 2\tilde{v}_{N_r+1}^{N_r}) Q_{N_r}^n. \quad (C28)$$

Eq. (C28) can be expressed in a simpler form as:

$$u_{N_r-1}^{N_r} Q_{N_r-1}^{n+1} + u_{N_r}^{N_r} Q_{N_r}^{n+1} = v_{N_r-1}^{N_r} Q_{N_r-1}^n + v_{N_r}^{N_r} Q_{N_r}^n, \quad (\text{C29})$$

where

$$u_{N_r-1}^{N_r} = \frac{a_m \Delta \eta}{2 \Delta \rho \rho_{N_r}}; \quad u_{N_r}^{N_r} = 1 - \frac{a_m \Delta \eta}{2 \Delta \rho \rho_{N_r}}; \quad v_{N_r-1}^{N_r} = -\frac{a_m \Delta \eta}{2 \Delta \rho \rho_{N_r}}; \quad \text{and} \quad v_{N_r}^{N_r} = 1 + \frac{a_m \Delta \eta}{2 \Delta \rho \rho_{N_r}}. \quad (\text{C30})$$

Eqs. (C15), (C24) and (C29) can be combined to provide a propagation procedure that includes diffraction effects, which can be calculated as a solution of the following linear system of equations with a tri-diagonal matrix:

$$\mathbf{U} \mathbf{Q}^{n+1} = \mathbf{V} \mathbf{Q}^n, \quad (\text{C31})$$

where

$$\mathbf{Q}^* = [\mathcal{Q}_0^*, \dots, \mathcal{Q}_{j-1}^*, \mathcal{Q}_j^*, \dots, \mathcal{Q}_{N_r}^*]' \quad (\text{C32})$$

and

$$\mathbf{U} = \begin{bmatrix} u_0^0 & u_1^0 & & & & \\ u_0^1 & u_1^1 & u_2^1 & & & \\ & u_1^2 & u_2^2 & u_3^2 & & \\ & & \dots & & & \\ & & & u_{j-1}^j & u_j^j & u_{j+1}^j \\ & & & & \dots & \\ & & & & & u_{N_r-1}^{N_r} & u_{N_r}^{N_r} \end{bmatrix}. \quad (\text{C33})$$

The matrix  $\mathbf{V}$  can be expressed in a form analogous to that of the matrix  $\mathbf{U}$  in Eq. (C33). A conventional technique applicable to tri-diagonal matrix systems can be used to solve Eq. (C31) such as, e.g., an LU decomposition using forward- and back- substitution for a tri-diagonal system. A solution to a linear equation such as that in Eq. (C31) is stable, and a zero pivoting is not required for a matrix which has a diagonal dominance at its rows. A diagonal dominance condition can be expressed for a tri-diagonal matrix by the relationship as follows:

$$|u_j^j| > |u_{j-1}^j| + |u_{j+1}^j|. \quad (\text{C34})$$

Using the approximation  $\rho_j = j \Delta \rho$ , the condition provided in Eq. (C34) generally holds for the central and internal sample points:

$$|u_{j-1}^j| + |u_{j+1}^j| = \frac{a_m \Delta \eta}{2 \Delta \rho} \left( \left| \frac{1}{2j \Delta \rho} - \frac{1}{\Delta \rho} \right| + \left| \frac{1}{2j \Delta \rho} + \frac{1}{\Delta \rho} \right| \right) = \frac{a_m \Delta \eta}{\Delta \rho^2} < 1 + \frac{a_m \Delta \eta}{\Delta \rho^2} = |u_j^j|. \quad (\text{C35})$$

However, Eq. (C35) uses a constraint on incremental delta values used because of a condition at a boundary sample point:

$$\left| 1 - \frac{a_m \Delta \eta}{2 \Delta \rho \rho_{N_r}} \right| > \frac{a_m \Delta \eta}{2 \Delta \rho \rho_{N_r}}, \quad (C36)$$

which may be true if:

$$\left| \frac{a_m \Delta \eta}{2 \Delta \rho \rho_{N_r}} \right|_{\rho_{N_r}=1} = \frac{a_m \Delta \eta}{2 \Delta \rho} < 1, \quad (C37)$$

which can provide a constraint:

$$\frac{\Delta \eta}{\Delta \rho} < \frac{2}{a_m}. \quad (C38)$$

A solution to the propagation equation provided in Eq. (C7) uses a specification of an operator  $\Phi_\beta^Q(\eta + \Delta \eta, \tau)$ , which depends on an unknown  $\eta + \Delta \eta$  sample point. An iteration procedure should be applied, where this sample point at a current iteration is drawn from results of previous iterations. A determination of a subsequent sample point value for  $Q$  can be written as:

$$\mathbf{Q}^{n+1} \leftarrow \left( \begin{array}{c} \bar{\bar{\mathbf{N}}}_{i+1/2}^{n+1/2(k)} \xleftarrow{\Upsilon} \bar{\bar{\mathbf{N}}}_{i-1/2}^{n+1/2(k)} \\ \mathbf{Q}^{n+1(k+1)} \equiv \mathbf{Q}_{rd}^{n+1(k+1)} \xleftarrow[\Psi/2]{\Upsilon} \mathbf{Q}_r^{n+1(k+1)} \xleftarrow[\Phi]{\Upsilon} \mathbf{Q}_{\text{mid}}^n \end{array} \right)_{k=1 \dots K} \xleftarrow[\Psi/2]{\Upsilon} \mathbf{Q}^n (\equiv \mathbf{Q}^{n+1(1)}). \quad (C39)$$

According to Eqs. (C1)-(C3), an iteration step for the rate equation has a form:

$$\bar{\bar{\mathbf{N}}}_{n+1/2, i+1/2}^{(k)} \approx \exp(\Delta \tau \Upsilon^{\bar{Q}^{(k)}}[n]) \bar{\bar{\mathbf{N}}}_{n+1/2, i-1/2}^{(k)}, \quad (C40)$$

where

$$\Upsilon^{\bar{Q}^{(k)}}[n] = \Upsilon_0 + \sum_{\alpha=1}^{N_A} \Upsilon_\alpha^{\bar{Q}^{(k)}}[n], \quad (C41)$$

and

$$\Upsilon_\alpha^{\bar{Q}^{(k)}}[n] = D_\alpha \frac{1}{2} \left\{ \bar{Q}_{n,j,i}^\alpha + \bar{Q}_{n+1,j,i}^{(k)\alpha} \right\}. \quad (C42)$$

Each iteration involves applying three operations: applying the diffraction operator at  $k=0$  using Eq. (C43), applying polarization term using Eq. (C44) and applying the same diffraction effect using Eq. (C45). Eqs. (C43)-(C45) are written as

$$\mathbf{Q}_{\text{mid}}^n = \mathbf{U}^{-1} \mathbf{V} \mathbf{Q}^n, \quad (C43)$$

$$\mathbf{Q}_r^{n+1(k+1)} = \exp(-\Delta \eta \Phi_L) \prod_{\beta=1}^{N_B} \exp\left(\Delta \eta \Phi_\beta^{N^{(k)}}[n+1/2, i-1/2] \Phi_\beta^{Q^{(k)}}[n]\right) \mathbf{Q}_{\text{mid}}^n, \quad (C44)$$

and

$$\mathbf{Q}^{n+1(k+1)} \equiv \mathbf{Q}_{rd}^{n+1(k+1)} = \mathbf{U}^{-1} \mathbf{V} \mathbf{Q}_r^{n+1(k+1)}, \quad (C45)$$

where the following discrete forms of propagation operators  $\Phi_\beta^N(\eta, \tau)$  and  $\Phi_\beta^Q(\eta, \tau)$  are used:



$$\Phi_{\beta}^{N^{(k)}}[n+1/2, i-1/2] \equiv \sigma_{\beta} \cdot \left\{ \frac{\mathbf{N}_{n+1/2, j, i-1/2}^{(k)} + \mathbf{N}_{n+1/2, j, i+1/2}^{(k)}}{2} \right\}, \quad (\text{C46})$$

$$\Phi_{\beta}^{Q^{(k)}}[n] \equiv \frac{\bar{Q}_{n, j, i}^{\beta-1} + \bar{Q}_{n+1, j, i}^{(k)\beta-1}}{2}, \quad (\text{C47})$$

and

$$\Phi_L \equiv c. \quad (\text{C48})$$

A computational procedure for determining the propagation of an electromagnetic pulse in a nonlinear absorbing material which accounts for diffraction effects are described using the following equations. Based on Eqs. (C1)-(C2), or (C40)-(C42), a rate equation are used which have the following form:

$$\begin{aligned} \bar{\bar{\mathbf{N}}}_{n+1/2, i+1/2}^{(k)} &\approx \exp \left( \Delta \tau \left\{ \Upsilon_0 + \sum_{\alpha=1}^{N_A} \Upsilon_{\alpha}^{\bar{Q}^{(k)}}[n] \right\} \right) \bar{\bar{\mathbf{N}}}_{n+1/2, i-1/2}^{(k)} \\ &= \exp \left( \iota_0 + \sum_{\alpha=1}^{N_A} \iota_{\alpha} \frac{\{\bar{Q}_{n, j, i}^{\alpha} + \bar{Q}_{n+1, j, i}^{(k)\alpha}\}}{2} \right) \bar{\bar{\mathbf{N}}}_{n+1/2, i-1/2}^{(k)}, \end{aligned} \quad (\text{C49})$$

with

$$\iota_0 \equiv \Delta \tau T_0 \tilde{D}_0, \text{ and } \iota_{\alpha} \equiv \Delta \tau T_0 \frac{\tilde{D}_{\alpha}}{\alpha \hbar \omega_0} (2nc_0 Q_0^2)^{\alpha}. \quad (\text{C50})$$

Using the results provided in Eqs. (C43)-(C48) a mathematical expression to describe propagation of a pulse can be written in the following form:

$$\mathbf{Q}^{n+1(1)} \equiv \mathbf{Q}^n, \text{ ; } \mathbf{Q}_{\text{mid}}^n = \mathbf{U}^{-1} \mathbf{V} \mathbf{Q}^n; \quad (\text{C51})$$

$$\mathbf{Q}_r^{n+1(k+1)} = \exp \left( - \sum_{\beta=1}^{N_B} \Phi_{\beta} \cdot \left\{ \frac{\mathbf{N}_{n+1/2, j, i-1/2}^{(k)} + \mathbf{N}_{n+1/2, j, i+1/2}^{(k)}}{2} \right\} \left\{ \frac{\bar{Q}_{n, j, i}^{\beta-1} + \bar{Q}_{n+1, j, i}^{(k)\beta-1}}{2} \right\} - \phi_L \right) \mathbf{Q}_{\text{mid}}^n; \quad (\text{C52})$$

$$\mathbf{Q}^{n+1(k+1)} \equiv \mathbf{Q}_{rd}^{n+1(k+1)} = \mathbf{U}^{-1} \mathbf{V} \mathbf{Q}_r^{n+1(k+1)}; \quad (\text{C53})$$

with

$$\Phi_{\beta} \equiv \Delta \eta L_{df} N (2nc_0 Q_0^2)^{\beta-1} \tilde{\sigma}_{\beta}; \quad \phi_L \equiv \Delta \eta \tilde{c} L_{df}. \quad (\text{C54})$$

By introducing a parameter  $\xi = \frac{a_m \Delta \eta}{\Delta \rho^2}$  the nonzero elements of internal rows of matrices  $\mathbf{U}$  and

$\mathbf{V}$ , i.e.  $u_j^i$  and  $v_j^i$  such that  $i \in \{1, \dots, N_r\}$  and  $j \in \{i-1, \dots, i+1\}$ , can be written as:

$$u_{j-1}^j = \frac{\xi}{2} \left( \frac{1}{2j} - 1 \right); \quad (\text{C55})$$

$$u_j^j = 1 + \xi; \quad (\text{C56})$$

$$u_{j+1}^j = -\frac{\xi}{2} \left( \frac{1}{2j} + 1 \right) ; \quad (C57)$$

$$v_{j-1}^j = -u_{j-1}^j ; \quad (C58)$$

$$v_j^j = 1 - \xi = 2 - u_j^j ; \quad (C59)$$

and

$$v_{j+1}^j = \frac{\xi}{2} \left( \frac{1}{2j} + 1 \right) = -u_{j+1}^j . \quad (C60)$$

By applying Eq. (C25), the nonzero elements of the first rows of matrices  $\mathbf{U}$  and  $\mathbf{V}$ , i.e.  $u_j^i$  and  $v_j^i$  such that  $i = 0$  and  $j \in \{0, 1\}$ , can be written as:

$$u_0^0 = 1 + 2\xi ; \quad (C61)$$

$$u_1^0 = -2\xi ; \quad (C62)$$

$$v_0^0 = 1 - 2\xi = 2 - u_0^0 ; \quad (C63)$$

and

$$v_1^0 = 2\xi = -u_1^0 . \quad (C64)$$

By applying Eq. (C30), the nonzero elements of the last rows of matrices  $\mathbf{U}$  and  $\mathbf{V}$ , i.e.  $u_j^i$  and  $v_j^i$  such that  $i = N_r$  and  $j \in \{N_r - 1, N_r\}$ , can be written as:

$$u_{N_r-1}^{N_r} = \frac{\xi}{2N_r} ; \quad (C65)$$

$$u_{N_r}^{N_r} = 1 - \frac{\xi}{2N_r} ; \quad (C66)$$

$$v_{N_r-1}^{N_r} = -\frac{\xi}{2N_r} = -u_{N_r-1}^{N_r} ; \quad (C67)$$

and

$$v_{N_r}^{N_r} = 1 + \frac{\xi}{2N_r} = 2 - u_{N_r}^{N_r} . \quad (C67)$$